
Coastal Engineering Journal

ISSN: (Print) (Online) Journal homepage: https://www.tandfonline.com/loi/tcej20

# Numerical extensions to incorporate subgrid corrections in an established storm surge model

Amirhosein Begmohammadi, Damrongsak Wirasaet, Autumn Poisson, Johnathan L. Woodruff, J. Casey Dietrich, Diogo Bolster & Andrew B. Kennedy

**To cite this article:** Amirhosein Begmohammadi, Damrongsak Wirasaet, Autumn Poisson, Johnathan L. Woodruff, J. Casey Dietrich, Diogo Bolster & Andrew B. Kennedy (2023) Numerical extensions to incorporate subgrid corrections in an established storm surge model, Coastal Engineering Journal, 65:2, 175-197, DOI: 10.1080/21664250.2022.2159290

**To link to this article:** https://doi.org/10.1080/21664250.2022.2159290

Published online: 28 Dec 2022.

COASTAL ENGINEERING JOURNAL
2023, VOL. 65, NO. 2, 175–197
https://doi.org/10.1080/21664250.2022.2159290



# Numerical extensions to incorporate subgrid corrections in an established storm surge model

Amirhosein Begmohammadi[a], Damrongsak Wirasaet[a], Autumn Poisson[b], Johnathan L. Woodruff[b], J. Casey Dietrich[b], Diogo Bolster[a] and Andrew B. Kennedy[a]

[a]Environmental Fluid Dynamics, Department of Civil and Environmental Engineering and Earth Sciences, University of Notre Dame, Notre Dame, Indiana, USA; [b]Department of Civil, Construction, and Environmental Engineering, North Carolina State University, Raleigh, NC, USA

**ABSTRACT**
Inundation models represent coastal regions with a grid of computational points, often with varying resolution of flow pathways and barriers. Models based on coarse grid solutions of shallow water equations have been improved recently via the use of subgrid corrections, which account for information (ground surface elevations, roughness characteristics) at smaller scales. In this work, numerical approaches of an established storm surge model are extended to include subgrid corrections. In an attempt to maintain continuity with existing users and results, model extensions were limited to those needed to provide basic subgrid capabilities, and included two major additions. First, a finite volume method is used to incorporate corrections to the mass and momentum equations using high-resolution ground surface elevations. Second, the no-slip condition imposed on the B-grid wet/dry interface in the model is modified to a slip condition to enable flows in channels with widths comparable to cell size. Numerical results demonstrate these numerical extensions can significantly enhance the accuracy of the model's predictions of coastal flooding, with low additional computational cost.

**ARTICLE HISTORY**
Received 17 June 2022
Accepted 11 December 2022
Published online

**KEYWORDS**
Subgrid model; storm surge modeling; numerical method; SLOSH; mathematical modeling

## 1. Introduction

Storm surge is a rise in water above the normal astronomical tide and can cause extensive flooding in areas with a relatively flat coastal topography (Hope et al. 2013), leading to loss of life and property damage. In one of the largest storm surges in history, Hurricane Katrina in 2005 caused catastrophic damage of nearly $125 billion to Louisiana and Mississippi, USA, with 1,833 confirmed fatalities (Corelogic, 2020). While less severe in their effects, many recent storms have caused flooding and damages along the U.S. Atlantic and Gulf coasts (Park 2021). Accurate and efficient predictions of storm surge are essential to save lives and protect properties in coastal regions.

Storm surge and coastal flooding can be modeled via numerical solutions of the two-dimensional (2-D), depth-averaged, Shallow Water Equations (SWE). In these models, ground surface elevations and other information are represented at the grid/mesh level, by approximating their values at the center, edges, or vertices of a computational cell.

To improve accuracy, the grid resolution can be increased, but with a corresponding increase in computational time. One alternative approach to improve models of shallow water hydrodynamic problems is to use subgrid models (Bates 2000; Casulli 2009; Defina 2000). These models use information at smaller scales in the model formulation to correct the behavior of flow variables (water levels, current velocities) at the grid scale. They have gained attention because of their abilities to improve accuracy and efficiency on a coarsened grid.

The early subgrid models for SWE-based modeling were introduced by Roig (1989), Defina, D'Alpaos, and Matticchio (1994), Defina (2000), and King (2001), where an artificial porosity (introduced as a function of water surface elevation) was proposed to account for partially wet areas. Casulli (2009) proposed a semi-implicit, finite volume-finite difference approach on a staggered grid with a novel wetting/drying algorithm by utilizing the porosity function to guarantee the positivity of the water height and to account for partially wet cells. This method can be applied on relatively coarse grids while it incorporates high-resolution bathymetric data at the subgrid level. Casulli and Stelling (2011) and Sehili, Lang, and Lippert (2014) applied this method to study flows in Venice Lagoon and the Elbe River, respectively, and showed that the subgrid model enhances performance with minimal additional computational cost. Stelling (2012) presented an approach for flood simulations that combined the subgrid wetting/drying approach of Casulli (2009) with the correction of bottom friction based on the concept of roughness depth within a fully finite-volume framework and a quadtree grid approach for

**CONTACT** Amirhosein Begmohammadi abegmoha@alumni.nd.edu

local grid refinement. Similarly, based on Casulli's subgrid formulation, Volp, Van Prooijen, and Stelling (2013) developed a finite-volume, subgrid formula with an assumption of constant friction slope flows at the subgrid level, leading to revised formulations of bottom friction and advection terms in the momentum equation. More recently, by using the volume averaging technique, Kennedy et al. (2019) proposed an upscaled form of the 2D SWEs for storm surges. The upscaled system of equations is structurally similar to the standard SWEs, but has additional terms/coefficients related to integral properties of the fine-scale topography and flow.

Although some subgrid approaches, e.g. Defina (2000) and Kennedy et al. (2019), were derived generally, many of these studies, e.g. Casulli (2009) and Volp, Van Prooijen, and Stelling (2013), were devised within a framework of numerical methods chosen to be suitable for subgrid corrections. However, in practice, technical challenges and ambiguities may arise in the implementation of subgrid corrections in established models, which often use numerical methods that are less amenable to define averaging areas and related aspects required for the subgrid corrections. Despite these challenges, adapting subgrid approaches into widely used models has appeal, because models' software infrastructures can be readily leveraged. Woodruff et al. (2021) implemented the upscaled SWEs with the mass and friction corrections in the finite-element-based, shallow water, ADvanced CIRCulation (ADCIRC) model. The challenging part of that implementation was to represent the averaged flow variables for an unstructured, triangular mesh within a continuous-Galerkin, finite-element framework, due to its vertex-based arrangement of flow variables. This challenge was addressed via the use of representative areas for both elements and vertices. Through a number of test cases, including realistic inundation induced by Hurricane Rita in 2005, they showed that the subgrid corrections can improve the numerical performance of coarse grid models, i.e. yielding predictions of coastal water levels that were similar in accuracy to, but 10 to 50 times faster than, fine-grid models.

For real-time forecasting, the Sea, Lake, and Overland Surges from Hurricanes (SLOSH) model has been developed and applied by the U.S. National Weather Service (NWS) to estimate storm surge heights resulting from hurricanes (Jelesnianski 1992). SLOSH uses a unique variant of 2D SWEs and discretizes them using an explicit, finite-difference formula on a staggered B-grid with, in some model conditions, C-grid cells in small portions of a model domain for a subgrid treatment of small features such as subgrid channels (hand coding is required in specifying such the cells in the model input files) (For the B-grid, the surface elevation is located at the cell center and both transport components are placed at the corner of the cells; for the C-grid, the surface elevation is placed at the cell center and the transport components are located at the midpoint of the cell edges (Arakawa and Lamb 1977)). The equations are solved on a polar, elliptic, or hyperbolic grid, telescopic outward with a finer resolution near the center (coastline), to estimate storm surge accurately (Jelesnianski 1992). SLOSH storm surge predictions depend strongly on accurate meteorological input such as hurricane size, intensity, forward speed, trajectory, and atmospheric pressure (Forbes et al. 2014). SLOSH-based models are computationally efficient and are used for ensembles of predictions in real-time and for climatological surge studies (Forbes et al. 2014; Glahn et al. 2009; Zachry et al. 2015).

In this study, we adapt the numerical implementation of SLOSH. The goal is not to completely rewrite this established model, which would certainly be much different if created today, but instead to maintain continuity with existing SLOSH results in the open ocean while extending formulations to improve inundation performance, particularly in regions with narrow channels. Accomplishing this goal requires two significant modifications/extensions. First, the existing no-slip boundary conditions for transport – imposed when at least one of the four cells surrounding a transport node is dry – are changed to slip conditions, which allow transport in narrow channels. This extension provides a platform to implement the model without predetermining the flow paths. Second, subgrid corrections are incorporated to improve the accuracy of the model. A finite-volume formula is introduced to account for high-resolution bathymetry variations on a subgrid level. It provides a platform to automatically take high-resolution bathymetric data and produce polar, elliptical, or curvilinear grids without hand coding. Section 2 describes the model formulation with the inclusion of subgrid corrections, while section 3 assesses the performance of the developed model by using test cases ranging from an idealized set-up to realistic applications of storm surge induced by Hurricanes Florence in 2018. Finally, section 4 summarizes the present work and discusses a framework for future research and development.

## 2. Methodology

### 2.1. Governing equations

The shallow water equations (SWEs) describe flows in various coastal and environmental engineering problems, such as estuarine circulation, tides, and storm surges. The SWEs can be solved in a variety of ways, such as 1D or 2D, conservative or non-conservative forms of momentum equations (Canestrelli and Toro 2012; Dresback, Kolar, and Casey Dietrich 2005).

#### 2.1.1. Equations of motion on a Cartesian framework

The SLOSH storm surge model uses the following form of SWEs in the Cartesian frame of reference (Jelesnianski 1992). The continuity is described as:

$$\frac{\partial h}{\partial t}+\frac{\partial U}{\partial x}+\frac{\partial V}{\partial y}=0 \tag{1}$$

where U and V are components of transport in $x$ and $y$ direction, respectively, and $h$ is the free surface elevation.

Platzman (1963) derived the equations of motion for storm surge computations in the Cartesian framework. Then, these equations were modified with a bottom slip coefficient, to give the form of transport equations (Jelesnianski 1992) for storm surge modeling:

$$\begin{aligned}\frac{\partial U}{\partial t}=&-gH(B_r\frac{\partial(h-h_0)}{\partial x}-B_i\frac{\partial(h-h_0)}{\partial y})\\&+f(A_rV+A_iU)+C_rx_\tau-C_iy_\tau,\end{aligned} \tag{2}$$

$$\frac{\partial V}{\partial t}=-gH(B_r\frac{\partial(h-h_0)}{\partial y}-B_i\frac{\partial(h-h_0)}{\partial x}) \tag{3}$$

where $h_0$ is the hydrostatic water height due to surface pressure, $f$ is Coriolis parameter, $y_\tau$ and $x_\tau$ are components of surface stress, $A_i$,$A_r$,$B_i$,$B_r$, $C_i$, $C_r$ are bottom stress terms, and $H=h+D$ denotes the total depth with $D$ being the depth of the quiescent water relative to the reference datum. Note that the coefficients $A_i$, $A_r$, $B_i$, $B_r$, $C_i$, and $C_r$ belong to terms derived from "formally" solving the shallow water equation with the vertical mixing term. See p. 741–743 of Jelesnianski (1967) and Appendix A of Jelesnianski (1992) for the full detailed account on the derivation of the bottom friction terms (For a self-contained purpose, we also briefly summarize such the derivation in Appendix A). These coefficients are defined through the water depth, vertical mixing eddy viscosity coefficient, "slip" bottom coefficient, and the Coriolis parameter. They are different from those used in studies based on the traditional shallow water equations, where bottom stress is assumed to obey a quadratic friction law.

A constant drag coefficient in air and a constant eddy stress coefficient in the water are used due to the difficulty of forecasting winds surrounding a hurricane. (For more details, see Jelesnianski (1992).)

#### 2.1.2. The equations of motion on a polar frame of reference

A polar or elliptical/hyperbolic telescopic grid type is selected for efficiency purposes in the SLOSH model (For more detail, see Conver et al. (2008)). This type of grid is telescopic outward of the center, allowing a finer resolution near the coastline, where the topography variation is essential and monotonically increased toward the open ocean, implying a lower resolution offshore. For computational benefits, the equations of motion are transformed from Cartesian to non-Cartesian coordinates. Although the transformed equations emerge more complicated than the non-transformed equations, the transformed equations have useful properties in terms of the numerical method for the simple and efficient computations when a polar or elliptical/hyperbolic telescopic grid are used.

For simplicity of the presentation, we consider the governing equations in the polar frame of reference with the following transformation (Jelesnianski 1992):

$$P=\ln(r/R_0),\ Q=\theta \tag{4}$$

is considered (see Jelesnianski (1992) for governing equations in a general conformal transformation). In the above formula, $R_0$ is a scale that controls the stretching of the grid, and $r$ and $\theta$ are the distance from the origin and angle between the line from origin to the point, respectively. This transformation maps a uniform grid in the $P$-$Q$ coordinate system to a telescopic polar grid in the physical domain.

Using the transformation in Equation (4), one can write the transformation of the Equations (1), (2), and (3) in the $P$-$Q$ coordinates as (for more detail, see Jelesnianski (1992)):

$$\frac{\partial H}{\partial t}+\frac{1}{r^2}\left(\frac{\partial U}{\partial P}+\frac{\partial V}{\partial Q}\right)=0, \tag{5}$$

$$\begin{aligned}\frac{\partial U}{\partial t}=&-gH\left(B_r\frac{\partial h}{\partial P}-B_i\frac{\partial h}{\partial Q}\right)+\\&f(A_rV+A_iU)+r(\cos(\theta)X_T+\sin(\theta)Y_T),\end{aligned} \tag{6}$$

$$\begin{aligned}\frac{\partial V}{\partial t}=&-gH\left(B_r\frac{\partial h}{\partial Q}-B_i\frac{\partial h}{\partial P}\right)-\\&f(A_rU-A_iV)+r(\cos(\theta)Y_T-\sin(\theta)X_T),\end{aligned} \tag{7}$$

where

$$X_T=-gH(B_r\frac{\partial h_0}{\partial P}-B_i\frac{\partial h_0}{\partial Q})+C_rx_\tau-C_iy_\tau, \tag{8}$$

$$Y_T=-gH(B_r\frac{\partial h_0}{\partial Q}-B_i\frac{\partial h_0}{\partial P})+C_ry_\tau+C_ix_\tau, \tag{9}$$

where $U=r\cos(\theta)\mathrm{U}+r\sin(\theta)\mathrm{V}$ and $V=-r\sin(\theta)\mathrm{U}+r\cos(\theta)\mathrm{V}$. The transformed form of Equations (5), (6), (7) are structurally similar to the equations in Cartesian coordinates (1), (2), (3) except for new coefficients and source terms.

These equations have three unknown solution variables $U(P,Q,t)$, $V(P,Q,t)$, and $h(P,Q,t)$. Note that the continuity Equation (5) is written with the time rate of change of the total water depth $\partial H/\partial t$, instead of $\partial H/\partial t$ as originally considered in Jelesnianski (1992). Although these terms are equivalent on the

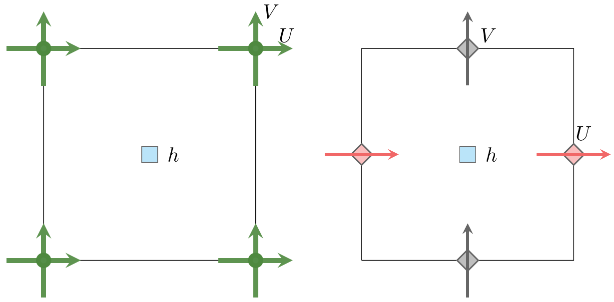


Figure 1. Arrangement of solution variables in a single cell for the staggered B-grid (left) and C-grid (right). Light blue squares are the location of surface elevation $h$. Green circles show the location of transport components ($U$ and $V$) on the staggered B-grid. Red and gray diamonds show the locations of $U$ and $V$ transport components, respectively, on the staggered C-grid.

continuous level (because the bathymetric depth $D$ is time-independent), the form in Equation (5) permits an inclusion of subgrid partial filling of water in a computational cell. (This aspect will be apparent in section 2.2.)

To solve the SWEs numerically on the uniform grid, different types of staggered grids can be considered (Arakawa and Lamb 1977). Two widely used grid arrangements are a staggered B-grid and a staggered C-grid (Figure 1). In the C-grid, the $U$ and $V$ components of the transports are placed at the midpoints of cell edges normal to the component directions, and the water surface elevation is defined at the cell center. For the B-grid, the water surface elevation is also defined at the cell center, but both $P$ and $Q$ components of the transports are defined at the cell corners. In the SLOSH model, Equations (5)–(7) are discretized mainly on a staggered B-grid. In some setups, the model utilizes a staggered C-grid locally to capture the effects of narrow channels. Staggered C-grid cells in such setups are predetermined in the grid. In the subsequent sections, finite-volume schemes of Equations (5)–(7) accounting for subgrid bathymetry on the B-grid are presented. In section 2.2.5, an implementation of slip boundary conditions on the B-grid is introduced to avoid predetermining C-grid cells.

## 2.2. Model description

Here, we aim to accommodate the subgrid corrections in the equations of motion (5)–(7) by using a finite volume method on a staggered B-grid, in which the unknown water surface elevation $h$ is placed at the cell center and the unknown transport components $U$ and $V$ are placed in the corner of cells ($h^k_{m,n} = h(m\Delta P, n\Delta Q, k\Delta t)$, $U^k_{m,n} = U((m-\frac{1}{2})\Delta P, (n-\frac{1}{2})\Delta Q, k\Delta t)$, $V^k_{m,n} = V((m-\frac{1}{2})\Delta P, (n-\frac{1}{2})\Delta Q, k\Delta t)$). The continuity Equation (5) and transport Equations (6), and (7) will be integrated over their associated control volumes depicted in Figure 2.

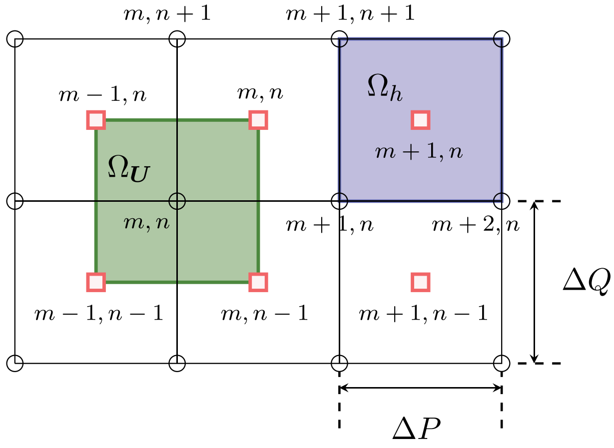


Figure 2. Schematic of the finite volume method on a staggered B-grid. Red squares and black circles show the locations of cell centers and cell corners for discretization of the surface elevation and transport components, respectively. $\Omega^h$ and $\Omega^U$ are the control volume associated with the water surface elevation and transport components, respectively.

### 2.2.1. Subgrid resolution

For a given bathymetric depth function $D(P,Q)$, the auxiliary porosity function is expressed by:

$$\phi(P,Q,z) = \begin{cases} 0 & D(P,Q)+z \le 0 \\ 1 & D(P,Q)+z > 0 \end{cases}, \tag{10}$$

where $z \in (-\infty, \infty)$ for a given elevation $z$. This function can be used to precisely express the flow domain within the FV cell from $D(P,Q)$ and the surface elevation (Casulli 2009). The wet area of $\Omega^h_{m,n}$ corresponds to the horizontal integral of this auxiliary function at free surface $z = h_{m,n}$

$$\phi_{m,n}(h_{m,n}) = \int_{\Omega^h_{m,n}} \phi(P,Q,h_{m,n})\mathrm{d}P\mathrm{d}Q. \tag{11}$$

The total water depth at a point $(P,Q)$ within the cell $\Omega_{m,n}$ is the vertical integral of this function from $-\infty$ to the free surface elevation, i.e.

$$\begin{aligned} H(P,Q,h_{m,n}) &= \int_{-\infty}^{h_{m,n}} \phi(P,Q,z)\mathrm{d}z \\ &= \max(0, D(P,Q)+h_{m,n}). \end{aligned} \tag{12}$$

Note that the value of $H(P,Q,h_{m.n})$ is greater or equal to zero. The wet area within the cell is described by $\Omega^{h,w}_{m,n} = \{(P,Q) \mid H(P,Q,h_{m,n}) > 0\}$ and $|\Omega^{h,w}_{m,n}| = \phi_{m,n}(h_{m,n})$. The water volume of the $(m,n)$ cell can be determined by:

$$\begin{aligned} V_{m,n}(h_{m,n}) &= \int_{\Omega^h_{m,n}} H(P,Q,h_{m,n})\mathrm{d}P\mathrm{d}Q \\ &= \int_{z=-\infty}^{z=h_{m,n}} \phi_{m,n}(z)\mathrm{d}z. \end{aligned} \tag{13}$$

It can be verified that $V_{m,n} \ge 0$ and $0 \le \phi_{m,n} \le |\Omega_{m,n}|$.

In addition, we also account for the wet area and wet volume within the transport control volume in a finite volume discretization of the momentum equations (to be described in section 2.2.3). These quantities are defined similarly to that described above. More specifically, in the transport control volume ($\Omega^{\mathbf{U}}_{m,n}$), the wet area and the water volume are determined by

$$\widehat{\phi}_{m,n}(\widehat{h}_{m,n}) = \int_{\Omega^{\mathbf{U}}_{m,n}} \phi\left(P, Q, \widehat{h}_{m,n}\right) \mathrm{d}P\mathrm{d}Q, \qquad (14)$$

in which the hat superscript is used to emphasize that these quantities are associated with the transport control volume, and

$$\widehat{V}_{m,n}\left(\hat{h}_{m,n}\right) = \int_{\Omega^{\mathbf{U}}_{m,n}} H\left(P, Q, \hat{h}_{m,n}\right) \mathrm{d}z = \int_{z=-\infty}^{z=\hat{h}_{m,n}} \hat{\phi}_{m,n}(z) \mathrm{d}z \qquad (15)$$

where $\widehat{h}_{m,n}$ is the surface elevation at the $(m,n)$ cell corner, which is the average surface elevation of the surrounding wet cells.

In the above formulation, the local bed elevation $D(P,Q)$ is assumed to be known at all locations. In practice, bathymetric data are usually available in the form of DEMs, which must be finer than the computational grid resolution to implement this subgrid resolution.

### 2.2.2. Continuity discretization

We consider a fully explicit, finite-volume (FV) formula of the continuity equation for a cell $(m,n)$ that is obtained from integrating Equation (5) over the cell domain $\Omega^{h}_{m,n}$ and using an explicit Euler forward scheme for temporal discretization, more precisely,

$$\int_{\Omega_{m,n}} \frac{H^{k+1} - H^{k}}{\Delta t} \mathrm{d}P\mathrm{d}Q + \frac{1}{r^2_{m,n}} \left( \int_{(n+1/2)\Delta Q}^{(n+3/2)\Delta Q} U^k \mathrm{d}Q - \int_{(n-1/2)\Delta Q}^{(n+1/2)\Delta Q} U^k \mathrm{d}Q + \int_{(m+1/2)\Delta P}^{(m+3/2)\Delta P} V^k \mathrm{d}P - \int_{(m-1/2)\Delta P}^{(m+1/2)\Delta P} V^k \mathrm{d}P \right) = 0, \qquad (16)$$

where $H^k = H(P, Q, h^k_{m,n})$, $U^k$ and $V^k$ are the total water depth and transport components at time $t^k = k\Delta t$, and $r_{m,n}$ is the value of $r$ at the cell center. Applying (13) to the first two integrals and the trapezoidal rule to the edge integral terms yield:

$$\frac{V_{m,n}(h^{k+1}_{m,n}) - V_{m,n}(h^{k}_{m,n})}{\Delta t} + \frac{1}{r^2_{m,n}} \left( \frac{(U^k_{m+1,n+1} + U^k_{m+1,n})}{2} \Delta Q - \frac{(U^k_{m,n+1} + U^k_{m,n})}{2} \Delta Q + \frac{(V^k_{m+1,n+1} + V^k_{m,n+1})}{2} \Delta P - \frac{(V^k_{m+1,n} + V^k_{m,n})}{2} \Delta P \right) = 0, \qquad (17)$$

where $V_{m,n}\left(h^k_{m,m}\right)$ is the water volume in the cell $(m,n)$ determined from subgrid bathymetry and the surface elevation $h^k_{m,n}$. Dividing the above formula by $\Delta P \Delta Q / \Delta t$ and assuming that $\Delta P = \Delta Q = \Delta S$ (this is done for the sake of comparison below) results in the following scheme

$$\bar{V}_{m,n}\left(h^{k+1}_{m,n}\right) = \bar{V}_{m,n}\left(h^{k}_{m,n}\right) - \frac{\Delta t}{2 r^2_{m,n}\ \Delta S} \left( U^k_{m+1,n+1} - U^k_{m,n+1} + U^k_{m+1,n} - U^k_{m,n} + V^k_{m+1,n+1} + V^k_{m,n+1} - V^k_{m+1,n} - V^k_{m,n} \right) \qquad (18)$$

where $\overline{V}$ is the volume of a cell normalized by a cell area. Note that the finite difference discretization of the continuity equations in Jelesnianski (1992) is:

$$h^{k+1}_{m,n} = h^{k}_{m,n} - \frac{\Delta t}{2\ r^2_{m,n}\ \Delta S} \left( U^k_{m+1,n+1} - U^k_{m,n+1} + U^k_{m+1,n} - U^k_{m,n} + V^k_{m+1,n+1} + V^k_{m,n+1} - V^k_{m+1,n} - V^k_{m,n} \right) \qquad (19)$$

By comparing Equation (18) with Equation (19), it can be seen that the only difference is that the finite-volume formula considers $\overline{V}_{m,n}(h^{k+1}_{m,n})$ instead of $h^{k+1}_{m,n}$. Assuming high-resolution bathymetric data are available, this term ($\overline{V}_{m,n}(h^{k+1}_{m,n})$) represents the correct amount of water volume, based on the constant surface elevation, in the partially wet cells (compared to $(h_{m,n} + D_{m,n})\Delta P \Delta Q$ in the nonsubgrid formula).

### 2.2.3. Momentum discretization

Below we describe the discretization of the momentum equation in the $P$ direction (The discretization of the $V$ component is done in a similar manner). A finite-volume formula is obtained by integration of Equation (6) over the transport control volume cell $\Omega^{\mathbf{U}}_{m,n}$. To evaluate the resulted integral statement, the friction coefficients $B_r$, $B_f$, $A_r$, and $A_f$ are assumed constant over the control volume; the wind stresses exert on the wet portion of the control volume, and the gradients of the surface elevation are replaced by the following finite difference approximation:

$$\frac{\partial h}{\partial x} \approx \frac{h^k_{m,n} - h^k_{m-1,n} + h^k_{m,n-1} - h^k_{m-1,n-1}}{2\Delta P}, \qquad (20)$$

$$\frac{\partial h}{\partial y} \approx \frac{h^k_{m,n} + h^k_{m-1,n} - h^k_{m,n-1} - h^k_{m-1,n-1}}{2\Delta Q}. \qquad (21)$$

With an explicit Euler forward scheme in time, this leads to the following scheme

$$U^{k+1}_{m,n} = (1 + \Delta t f A_i) U^k_{m,n} - \left(F_{\mathrm{pre}}\right)_{m,n} + \Delta t f A_r V^k_{m,n} + r\Delta t \left( \cos(\theta)(X_T)^k_{m,n} + \sin(\theta)(Y_T)^k_{m,n} \right) \overline{\overline{\phi}}_{m+1,n}, \qquad (22)$$

where

$$\left(F_{\mathrm{pre}}\right)_{m,n} = -g\Delta t \overline{\overline{V}}_{m,n}(\hat{h}^k_{m,n}) \left( B_r \frac{h^k_{m,n} - h^k_{m-1,n} + h^k_{m,n-1} - h^k_{m-1,n-1}}{2\Delta P} - B_i \frac{h^k_{m,n} + h^k_{m-1,n} - h^k_{m,n-1} - h^k_{m-1,n-1}}{2\Delta Q} \right),$$

and

$$\overline{\overline{V}}_{m,n}(h^k_{m,n}) = \frac{\widehat{V}_{m,n}(h^k_{m,n})}{\Delta P \Delta Q}, \quad \overline{\overline{\phi}}_{m,n} = \frac{\widehat{\phi}_{m,n}(h^k_{m,n})}{\Delta P \Delta Q}.$$

The fully explicit, finite-difference discretization for the $U$ transport component on the B-grid presented in Jelesnianski (1992) is:

$$U_{m,n}^{k+1} = (1 + \Delta t f A_i)U_{m,n}^{k} - (F_{\text{pre}})_{m,n} + \Delta t f A_r V_{m,n}^{k} + r(\cos(\theta)(X_T)_{m,n}^{k} + \sin(\theta)(Y_T)_{m,n}^{k}), \quad (23)$$

where

$$(F_{\text{pre}})_{m,n} = -g\Delta t\overline{H}_{m,n}^{k}\left(B_r\frac{h_{m,n}^{k} - h_{m-1,n}^{k} + h_{m,n-1}^{k} - h_{m-1,n-1}^{k}}{2\Delta P} - B_i\frac{h_{m,n}^{k} + h_{m-1,n}^{k} - h_{m,n-1}^{k} - h_{m-1,n-1}^{k}}{2\Delta Q}\right)$$

with the total water depth

$$\overline{H}_{m,n}^{k} = \tfrac{1}{4}[(D_{m,n} + h_{m,n}^{k}) + (D_{m+1,n} + h_{m+1,n}^{k}) + (D_{m,n+1} + h_{m,n+1}^{k}) + (D_{m+1,n+1} + h_{m+1,n+1}^{k})].$$

Comparing the finite-volume (22) and finite-difference (23) discretization schemes, it can be seen that there are two main differences. First, the pressure term in the finite-volume formula considers the wet volume $\widehat{\overline{V}}_{m,n}(h_{m,n}^{k})$ instead of $\overline{H}_{m,n}^{k}$. Second, the wet fraction appears in the finite-volume formulation for external forces to consider partially wet area.

Note that, due to the use of the finite volume formulas for the discretization of both continuity and momentum equations, the term "FV/FV formula" is used to refer to the subgrid model.

### 2.2.4. Numerical solution

The approximate solution of $h^{k+1}$ can be obtained by solving Equation (18) in a cell-by-cell fashion. The procedure amounts to finding the value of $h^{k+1}$ so that $\overline{V}(h^{k+1}) = b$, where $b$ is the right-hand side of Equation (18) computed from the known surface elevation and transport components at the previous time step. In general, $\overline{V}(h)$ varies non-linearly with $h$ in the partially wet cells, and a root-finding method (such as the Newton-Raphson method) could be used to find the solution $h$. Here, to solve efficiently for $h^{k+1}$, we use a look-up table of the volume of the cells as a function of water surface elevation to find the water volume from a given $h$ and *vice versa*. In this approach, before the time marching step, the volume of a cell is pre-calculated for possible water surface elevations and stored in a computer memory for fast retrieval. During the time marching step of the mass equation, the pre-computed relationships are used to interpolate the value of the water surface elevation for a given volume (and vice versa when the volume is required for a given surface elevation). This procedure is computationally efficient because it relies on interpolation from a look-up table; in addition, it is independent of the resolution of the subgrid bathymetric DEM during the time marching step. The error associated with the use the lookup table corresponds to the error in the linear interpolation (see Figure 3 for illustration).

More specifically, in a forward look-up table, for a given $h_g$,

$$V(h_g) = V_l(h_g) + \frac{1}{2}\frac{d^2V(h)}{dh^2}(h_g - h_i)(h_g - h_{i+1}), \quad h_i \le h \le h_{i+1}.$$

where $V_L$ is the linear interpolation from $(h_i, V(h_i))$ and $(h_{i+1}, V(h_{i+1}))$ with $h_i \le h_g \le h_{i+1}$, the two consecutive data points in the look-up table. It follows directly that

$$|V(h_g) - V_l(h_g)| \le \frac{1}{8}\Delta h^2 \max_{h\in[h_i,h_{i+1}]}\left|\frac{d^2V(h)}{dh^2}\right|, h_g \in [h_i, h_{i+1}], \Delta h = h_{i+1} - h_i, \quad (24)$$

Similarly, in an inverse look-up table, for a given $V_g$

$$|h(V_g) - h_l(V_g)| \le \frac{1}{8}\Delta V^2 \max_{V\in[V_L,V_H]}\left|\frac{d^2h(V_g)}{dV^2}\right|, V \in [V_L, V_H], \Delta V = V_H - V_L. \quad (25)$$

In (24)-(25), $V(h)$ and $h(V)$ are assumed twice differentiable functions.

The transport component $U^{k+1}$ is obtained by solving Equation (22), and $V^{k+1}$ can be obtained in a similar manner. As done in the continuity equation, the wet area and wet volume of the transport cells are pre-computed and stored as a function of water surface elevation in look-up tables for efficient computation.

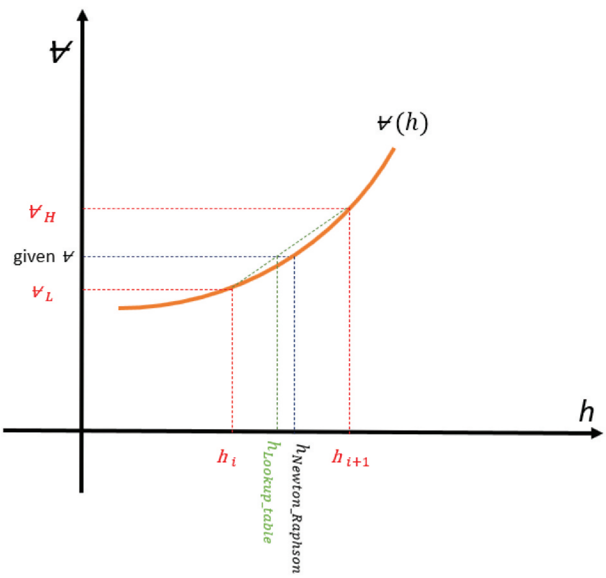


Figure 3. The volume as a function of the surface elevations. the Newton-Raphson solver yields a 'true' solution while the look up table approach yields an approximate solution where the interpolation error is the source of error. If interval levels ($\Delta h = h_{i+1} - h_i$) of the lookup table are small enough, it can safely assumed that the predicted surface elevations from the lookup table and the Newton–Raphson method are approximately equal.

### 2.2.5. Boundary condition on the borders of wet/dry edge cells

In SLOSH (Jelesnianski 1992), the transport components at a transport point in the B-grid are computed when all four cells surrounding the point are considered wet; they are set to zero otherwise. In other words, a no-slip condition is imposed on the boundaries of wet/dry cells. For a wet cell having two neighboring dry cells on its west and east edge/or its north and south edges, this strategy results in zero velocities at all its four corners. Therefore, without some remedies, the model does not permit flow through a channel of width smaller than the grid size (see Figure 4 for illustration). Note that alleviating this drawback is very important for the subgrid approach to perform well.

To solve this issue, the SLOSH model resorts to the use of cells with the C-grid arrangement locally in the portions of the grid where there is a narrow channel that cannot be represented properly with the B-grid and the no-slip condition. However, these C-grid cells must be predetermined at the model development phase.

In this work, as an alternative, we impose a slip condition on the wet/dry interface in the computational domain. This addition allows the governing equations to be solved on a fully staggered B-grid without having to predetermine any channels and small features at the model set-up stage. Figure 4 is used to illustrated this approach. By imposing the slip condition on the cell edges, the tangential components of transport at nodes along them are no longer zero and, as a result, allow the flow to go through the channel in the middle of the computational domain. This condition is implemented through setting the normal mass flux of wet/dry interface edges in Equation (18) to zero and using an extrapolated value of surface gradients from the wet sides in the discretization scheme of the momentum equation at nodes located on such interfaces. In addition, at nodes shared by two wet/dry interface edges running in the east/west or north/south direction (e.g. nodes $(m, n+1)$ and $(m+1, n)$ in Figure 4), only the transport component tangential to the segment formed by these two edges are computed, while the component perpendicular is set to zero; at nodes with three surrounding wet cells (e.g. node $(m, n)$), both $U$ and $V$ components are calculated, but, as shall be described below, only the certain transport component is used to update the surface elevation of cells surrounding the node.

We describe an implementation of the slip condition for a case depicted in Figure 5. This case considers a transport node $(m+1, n+1)$ shared by four cells of which only one $(m, n+1)$ cell is dry (for simplicity, we assume that, except the $(m, n+1)$ cell, cells neighboring the three wet cells are also wet). At the corner shared by three wet cells, the transport components $U$ and $V$ are computed. This corner node is part of the wet/dry boundary, and thus both transport components at this location, $U_{m+1,n+1}$ and $V_{m+1,n+1}$, are computed. These components are advanced in time (see (22) for the $U$ component) based on the approximate surface elevation gradient extrapolating from the wet sides

$$\frac{\partial h}{\partial P} \approx \frac{h_{m+1,n} - h_{m,n}}{\Delta P}, \quad \frac{\partial h}{\partial Q} \approx \frac{h_{m+1,n+1} - h_{m+1,n}}{\Delta Q}. \tag{26}$$

The water surface elevation of the cell $(m+1, n)$ is advanced as usual through Equation (18) by using both transport components at node $(m+1, n+1)$. For the $(m, n)$ and $(m+1, n+1)$ cell, only the transport components tangential to their respective wet–dry interface are used to compute the water surface elevation. The mass fluxes normal to the wet–dry interface of these cells are set to zero. More precisely, the schemes used to update the surface elevation of the $(m, n)$ and $(m+1, n+1)$ correspond to

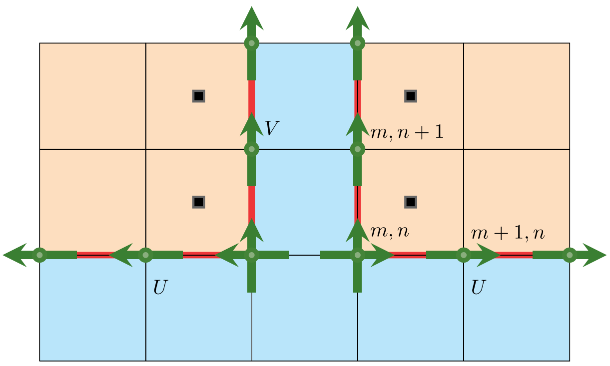


Figure 4. Wet area at grid level of a narrow channel in a staggered B-grid. Light blue cells are wet and light tan cells are dry. The thick red line shows the border of wet/dry cells. Green circles are transport points in wet/dry edges. Horizontal and vertical arrows denote $U$ and $V$ components of transports, respectively. With the no-slip conditions, the wet cells to which the channel belong have vanishing transport components at all four corners.

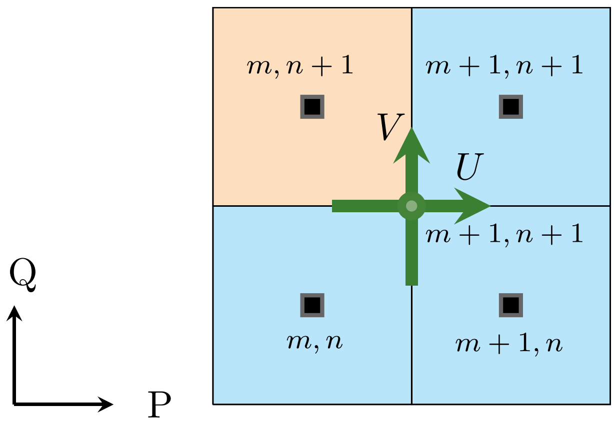


Figure 5. Schematic of transport computations at interface between wet (shown in light blue) and dry (shown in light tan) cells. The green circle shows the location of the $U$ and $V$ transport components in the boundary of wet/dry cells.

$$\overline{V}_{m,n}(h^{k+1}_{m,n}) = \overline{V}_{m,n}(h^k_{m,n}) - \frac{\Delta t}{r^2_{m,n}\Delta S}\left(U^k_{m+\frac{1}{2},n} - U^k_{m-\frac{1}{2},n} - V^k_{m,n-\frac{1}{2}}\right), \tag{27}$$

and

$$\overline{V}_{m+1,n+1}(h^{k+1}_{m+1,n+1}) = \overline{V}_{m+1,n+1}(h^k_{m+1,n+1}) - \frac{\Delta t}{r^2_{m+1,n+1}\Delta S}\left(U^k_{m+\frac{3}{2},n} + V^k_{m+1,n+\frac{3}{2}} - V^k_{m+1,n+\frac{1}{2}}\right), \tag{28}$$

respectively, where

$$U^k_{m+\frac{1}{2},n} := \frac{U^k_{m+1,n+1} + U^k_{m+1,n}}{2}, \text{ and } V^k_{m,n+1/2} := \frac{V^k_{m,n+1} + V^k_{m+1,n+1}}{2}. \tag{29}$$

### 2.2.6. Wetting/drying algorithm

The wetting/drying algorithm is applied on the continuity and momentum equations. Here, a cell is considered wet (active) when the surface elevation is greater than the minimum value of subgrid bed elevation ($h^k < -\max(b(x,y))$ and is considered dry otherwise. In our study, with wet/dry status of cells, the time marching is done in two steps as follows:

- First, update the surface elevation through the continuity equation. The following techniques are applied to compute surge values at future time $(k+1)$ at the center of the cell:

(1) If all four surrounding corners at the current time $k$ of a cell (four transport points) have no flow (i.e. zero transports), then computations are ignored at the center point, resulting in no change in the value of surface elevation of this cell.
(2) If the cell is wet and at least one of its surrounding corners at the current time $k$ has flow, Equation (18) is used to update the transport nodes.
(3) If computation at the center point results in negative $V(h^k)$ (i.e. $b$ in the right-hand side (RHS) of Equation (18) is negative), then the cell is set dry at future time $(k+1)$. Note that the negative water volume is not permitted; in order to prevent this, the transport at present time $(k)$ on the four corners is decreased by a fixed ratio to exhaust all water in the cell and no more, i.e. find $a$ such that the RHS in Equation (15) is zero:

$$V(h^k) - a\Delta t/(2r^2_{m,n}\Delta S)\left(U^k_{m+1,n+1} - \ldots - V^k_{m,n}\right) = 0; \tag{30}$$

the surface elevation of the such the cell at $k+1$ is then set to $-\max b(x,y)$, the minimum of subgrid bed elevation of the cell. Surface elevation at contiguous cells surrounding the four corners are computed (or recomputed) with the decreased transport values at the four corner points.

(4) If the cell is dry and at least one of the surrounding cells is wet (there are four surrounding cells), then two scenarios are plausible. First, if the minimum bathymetry of the dry cell is greater than the maximum surface elevation of surrounding wet cells, then the cell is considered dry. Second, suppose the maximum surface elevation of surrounding wet cells is greater than the minimum bathymetry of the cell. In that case, the cell is considered wet and has a thin layer of surface elevation to include in the calculation. In order to conserve mass, the values of the surface elevation of its surrounding wet cells are reduced accordingly.

- Second, update the transport components through the momentum equations. The momentum equations are applied after the surface elevation for the entire basin at the future time

$(k+1)$ is updated via the continuity equation. The following rules are applied for computations with momentum equations at corner of the cells:

(1) If all four surrounding cells are dry at future time $(k+1)$, transport is set to zero at future time $(k+1)$.
(2) If some cells are wet with at least two contiguous surrounding cells (cells that share border) are wet, the transport is calculated on the transport point at future time $(k+1)$ via an approach described in see Section 2.2.5.
(3) If all four surrounding cells are wet, Equation (22) is used to update the transport nodes.

### 2.2.7. Subgrid surface connectivity

The subgrid model introduced in Sections 2.2.1–2.2.4 aims to improve the accuracy of the model when using a relatively coarse grid. However, excessively coarse grids can allow artificial cross flows between disconnected areas separated by physical barriers smaller than the grid size. A number of approaches have been employed based on mesh refinement and edge blocking approaches (Hodges 2015; Zhi and Hodges 0000; b; Platzek et al. 2016) to deal with the subgrid surface connectivity issue. Casulli (2019) introduced a cell clone approach to eliminate an artificial cross-flow between disconnected regions within a cell without requiring further mesh refinement. Begmohammadi et al. (2021) extended the cell clone approach by breaking the cell clone into sub-clones to remove cross flow when barriers within the coarse grids are submerged to deal with the storm surge scenario. Splitting and merging sub-clones permits a more flexible performance of subgrid models to represent the effect of smaller scale barriers that are submerged and emerged at different water surface elevations.

One example of this type of scenario is barrier island chains, which can consist of several islands, and which may extend uninterrupted for more than a hundred kilometers. Generally, the effect of these narrow barriers cannot be captured by the presented subgrid model, if the island width is smaller than the grid size. Missing the effects of the barriers can lead to an overestimation of the water surface elevation when barriers should block the path. Here, a simple method is presented to represent the effects of the barrier islands on the coarse grid. First, the transport control volumes with barriers are identified. Second, the height of the barrier is determined by checking for the disconnected wet areas in a specific range of water surface elevations. (These two steps are done beforehand as a prepossessing step.) Third, during the time stepping, if the water surface elevation does not exceed the barrier height, the transport points are excluded in the calculation of the continuity equation. If the water surface elevation passes the height of the barrier, the transport points are activated. We depict the approach through Figure 6 which shows the barrier islands alongside the control volume over the mass cells and a transport cell.

To find the barrier's height, we first define a reasonable range of water surface elevations ($h_{\mathrm{Min}} < h < h_{\mathrm{Max}}$), based on extreme inundation and receding water levels for the computational domain. Starting from $h_b = h_{\mathrm{Max}}$, we check whether there is a path of connected pixels to reach from one wet edge of the control volume to the opposite wet edge of the control volume (i.e. from the west edge to the east edge and from the south edge to the north edge). If the connected path exists, the process is repeated for $h_b = h_b - \in$, ($\in = (h_{\mathrm{Max}} - h_{\mathrm{Min}})/\delta$, where $\delta$ is the number of the barrier's check levels) until there is no path of connected pixels from one edge to the opposite edge or reaching $h_b = h_{\mathrm{Min}}$. The value of $h_b$ at which this process terminates is considered the barrier's height. This new algorithm can be automated. Note that to implement this method, we take advantage of the existing SLOSH barrier to minimize coding.

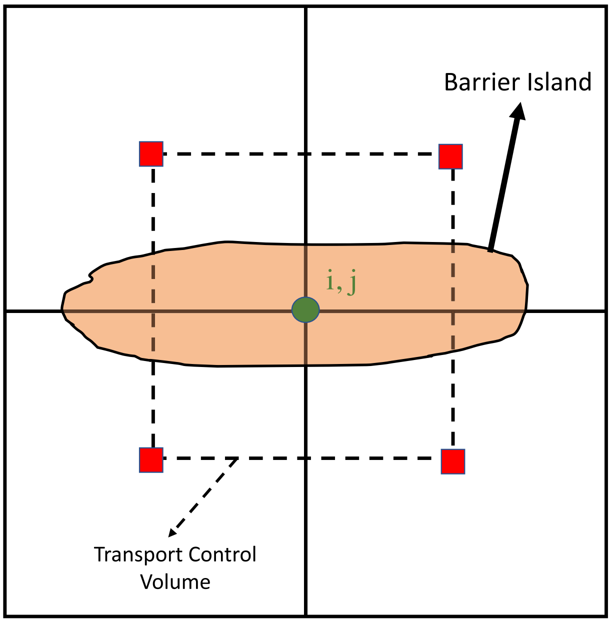


Figure 6. Schematic of how a barrier island (shown in tan) may affect the transport computations. Solid lines show the control volume over the mass cells, with red squares in the centers of the mass control volumes. Dashed lines show the control volume over the transport cell, with a green circle in the center of the control volume. At a certain water surface elevation when the barrier island splits the transport control volume into two separated areas that do not have a connection, the transport components are not calculated. When the water surface elevation exceeds the barrier height (i.e. barrier is submerged), then transport components are computed for the point with a barrier.

## 3. Tests and validation

Here, a set of test cases ranging from idealized domains to realistic settings are considered to demonstrate the ability of the subgrid model to represent the effects of features and channels that are smaller than the grid cell on a fully staggered B-grid, without resorting to using predetermined C-grid cells. Tests are divided into periodic flows in an idealized channel and bay system and a real storm on the North Carolina coast. The driving forces for the SLOSH model are the wind stress and the atmospheric pressure. In the idealized tests, the atmospheric pressure is assumed constant. For the realistic tests, a parametric wind model for hurricane-induced conditions is considered (see section 3.2.2). Telescopic polar grids (see Conver et al. (2008) for more details), where the grid cells are finer toward the center, are considered in all test cases.

### 3.1. *Idealized channel and bay system*

An idealized system (Figure 7) consists of an inner bay connected to an outer bay via a channel, where the outer main bay links to the open ocean. This system is used to show the ability of the present model to represent channels that are not resolved at the grid scale. We consider two configurations (A and B), in which the ground surface elevations are varied in the land portion within the domain. The high-resolution bathymetric data on which all calculations are based are described on a telescopic polar grid of 512 $\times$ 576 cells with the average grid spacing in the radial and tangential directions of $\Delta r = 0.2871$ km and $\Delta\theta =$

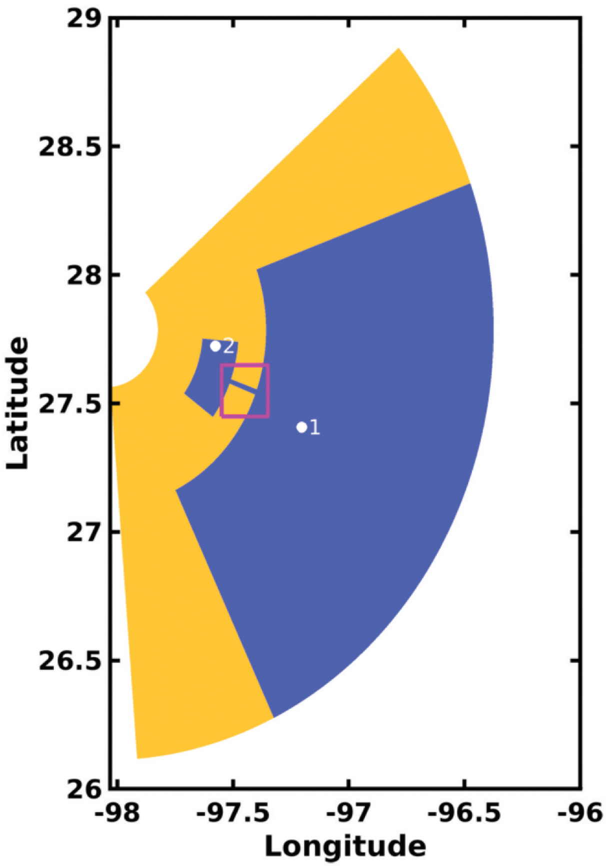


Figure 7. Bed elevations for the idealized bay channel test. Blue regions have a bed elevation of $-9.1440$ m, and yellow regions have a bed elevation of 15.2400 m for configuration a and 3.048 m for configuration B. The locations of stations 1 and 2 are indicated. Large arc shows the ocean side of the geometry.

0.3487 km, respectively. (Note that $\Delta\theta$ denotes the straight distance of arc ($r \times \delta\theta$) where $\Delta\theta$ is the angle spacing in radians.) Five (successively refined) grids (see Table 1 for more detail) are considered for simulations in configuration A, and three grid resolutions are considered for configuration B. The channel representation depends on the grid resolution (Figure 8). For the coarsest grid ($32 \times 36$ radial and tangential cells, respectively), the channel is located entirely within one strip of cells. For the next-coarsest grid ($64 \times 72$), the channel is represented partly within two cells in the tangential direction. For the finer grids, the channel is geometrically resolved. More specifically, there are 2, 4, and 8 cells across the channel in the tangential direction for grids $128 \times 144$, $256 \times 288$, and $512 \times 576$, respectively.

Wind stresses are the drivers for this test case, and the atmospheric pressure is constant. A time-varying, spatially constant wind coming alternately from the northwest and southeast directions (155.7365°N and 335.7365°N) is considered. A wind velocity and hence wind stress is assumed to be a sinusoidal function in time with a period of 10 hr and a maximum speed of 70.60 km/hr. This forcing produces fluctuations in surface water level of less than 0.6 m from an undisturbed water level, and flows connecting the bays occur only through the channel. A constant water surface elevation (a clamped boundary condition) is prescribed on the wet portion of the open boundary of the main bay. Tidal forcing is not considered in the simulations. Instead, a mean high water (MHW) elevation of $h = 0.3048$m is used as an initial condition, to mimic a typical procedure in SLOSH simulations in which the initial water surface elevation is adjusted to MHW.

### 3.1.1. Configuration A

In this configuration, the wet regions have a bed elevation of –9.14 m below mean sea level, and dry regions have a bed elevation of 15.24 m. The average bed elevation of the cells that include the channel over the coarse grid is 3.048 m for the coarser grids ($32 \times 36$ and $64 \times 72$), and thus conventional solution methods will predict dry regions throughout the channel. For each grid, two types of simulations are conducted. The first simulation is the conventional method, where SLOSH is run with the bathymetry of each cell being an average over a coarse grid and without the use of predetermined C-grid cells (i.e. the computations are performed entirely with the B-grid). The second simulation is the subgrid model with slip conditions, where the FV/FV formula presented in section 2.2 is used.

As expected, the time series of water surface elevations (Figure 9) from all simulations are in good agreement at Station 1, which is located in the open water where all grids can resolve the flow behavior. At Station 2, which is located in the secondary bay, and for the coarse grids ($32 \times 36$ and $64 \times 72$), the conventional method predicts water surface elevations with only minimal variations of about 5 cm from their mean values. This inaccuracy is caused by the channel not

Table 1. Grid statistics for the idealized bay and channel test case. Configuration A considers all five grid resolutions, while configuration B considers the two coarsest ($32 \times 36$ and $64 \times 72$) and finest ($512 \times 576$) grid resolutions. Note that straight distances are computed in radial and tangential directions, and the effects of grid curvatures are ignored for simplicity.

| Grid size (radial × tangential) | | (32 × 36) | (64 × 72) | (128 × 144) | (256 × 288) | (512 × 576) |
|---|---|---|---|---|---|---|
| Tangential $\Delta\theta$ (km) | Minimum | 0.921 | 0.448 | 0.216 | 0.105 | 0.051 |
| | Maximum | 14.581 | 7.646 | 3.922 | 1.989 | 1.007 |
| | Average | 5.404 | 2.673 | 1.386 | 0.696 | 0.349 |
| Radial $\Delta r$ (km) | Minimum | 0.915 | 0.440 | 0.213 | 0.104 | 0.049 |
| | Maximum | 15.105 | 7.858 | 4.013 | 2.022 | 1.020 |
| | Average | 4.487 | 2.210 | 1.143 | 0.573 | 0.287 |

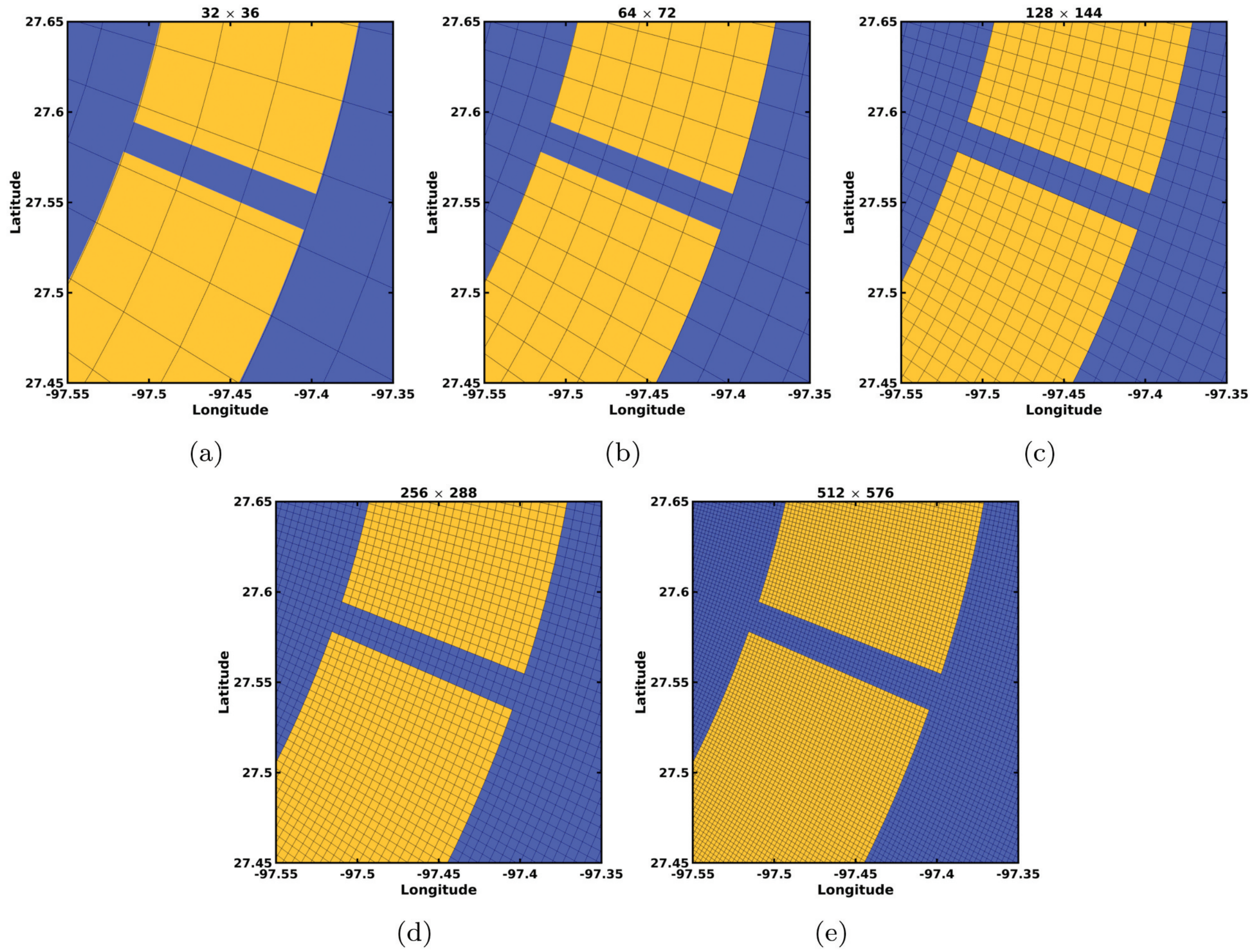


Figure 8. View of the area enclosed by the red square in Figure 7, for 5 grid sizes: a) grid resolution of 32 × 36 radial and tangential cells, respectively, b) grid resolution of 64 × 72, c) grid resolution of 128 × 144, d) grid resolution of 256 × 288, e) grid resolution of 512 × 576.

being resolved sufficiently to allow flow between bays. For the finer grids and the conventional method, the flow connectivity is resolved through the channel. For the conventional simulation on the 128 × 144 grid, the water surface elevations have an amplitude of about 0.5 m, although they are damped and phase-lagged relative to the results from the finest grids (256 × 288 and 512 × 576)), which have water surface elevations with an amplitude of about 0.7 m. For the subgrid model, the coarse grid calculations, 32 × 36 and 64 × 72, capture the hydrodynamic connectivity between two bays, with amplitudes of about 0.6 m and minimal phase lag, thus showing an improvement in accuracy relative to the conventional method.

The model performance is quantified via root-mean-square errors:

$$E_{\mathrm{RMS}} = \sqrt{\frac{1}{N}\sum_{i=1}^{N}\left(h(x,t^i) - h_{\mathrm{ref}}(x,t^i)\right)^2}, \qquad (31)$$

in which $N = 162$ is the number of water surface elevations in a time series, $h$ is a predicted water surface elevation, and $h_{\mathrm{ref}}$ is a reference water surface elevation (taken as the solution from the subgrid model on the finest 512 × 576 grid). The $E_{\mathrm{RMS}}$ values closer to zero represent better agreement with the reference solution. For the same grid resolution, the $E_{\mathrm{RMS}}$ values in the subgrid solution are lower than the conventional method for almost all cases. The largest differences are for the time series at Station 2 inside the inner bay. For the two coarser grids (32 × 36 and 64 × 72), the $E_{\mathrm{RMS}}$ values are one order of magnitude lower than those of the conventional solution. For the coarsest grid (32 × 36), the subgrid model has an $E_{\mathrm{RMS}} = 0.0805$ m, which is smaller than the conventional method for a grid with four times the resolution (128 × 144).

### 3.1.2. Configuration B

In this configuration, the wet regions have bed elevations identical to configuration A, but the dry regions have a bed elevation of only 3.05 m above mean sea level (Figure 7). For the 32 × 36 and 64 × 72 grids where the channel is under-resolved, the averaged bed elevation of cells containing the channel is $-3.0480$ m (compared to 15.24 m in Configuration A). These cells are flagged as wet

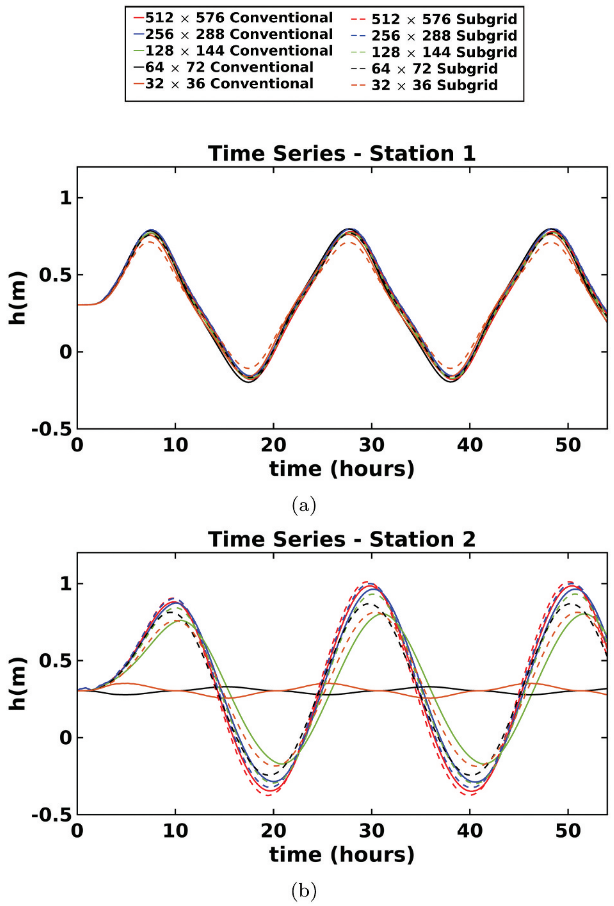


**Figure 9.** Time series of water surface elevations at stations a) 1 and b) 2 (with locations shown in Figure 7). Dashed lines shows the subgrid model, and solid lines show the conventional model.

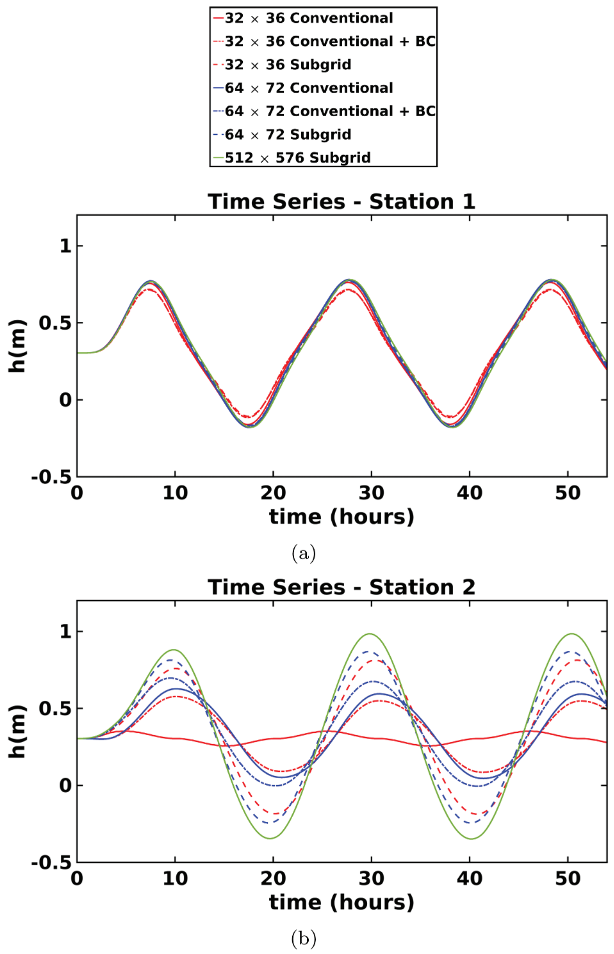


**Figure 10.** A) Time series of water surface elevations at stations a) 1 and b) 2 (with locations shown in Figure 7). Dashed lines shows the subgrid model, dotted lines show the conventional model with slip boundary condition, and solid lines show the conventional model.

cells in the conventional formulation (with the mean depth as their bathymetric depth), and the channel is part of the wet areas in the computational grids. (This is in contrast to Configuration A, where the conventional model flags the channel as dry for the two coarsest grids.) Note that, for the coarsest grid, each of these cells has two neighboring dry cells on its edges along the radial direction (a scenario similar to that depicted in Figure 4). Numerical results demonstrate an ability of the implemented slip boundary condition to remedy the shortcoming posed by the no-slip condition in this particular situation.

The two coarsest grids (32 × 36 and 64 × 72) and the finest grid (512 × 576) are used. In addition to the two types of simulations described in Configuration A, we also consider the conventional method with the slip boundary condition imposed on wet/dry boundaries (section 2.2.5).

The water surface elevations at Station 1, located in the open water in the main bay, have good agreement with the reference solution (Figure 10). However, the water surface elevations at Station 2 are predicted inaccurately for the coarse grids and conventional method (Figure 10). For the 32 × 36 grid, the conventional method predicts water surface elevations that again deviate by only about 5 cm from their mean values (It predicts identical results with configuration A). This inaccuracy, despite the channel being represented by cells with a positive flow depth, stems from the no-slip boundary condition on wet/dry cell edges, which prevent transport through the channel to the secondary bay.

The slip boundary condition allows transport through the channel. For the coarsest grid, this yields a much improved results of the water surface elevations with an amplitude of about 0.3 m. Using the subgrid model further improves the amplitudes to approximately 0.5 m. (It is worth mentioning that, for this particular test, if the no-slip condition is used in the subgrid approach, no gain over the conventional method is observed.)

Table 2 shows the $E_{RMS}$ errors relative to the high-resolution simulation (512 × 576 subgrid solution) for two coarse grids. Because the slip boundary condition allows transport through the channel, it has the effect of lowering the $E_{RMS}$ by a factor of about 2. The subgrid solution then lowers the $E_{RMS}$ by a factor of about 7 to 8, as its water surface elevations are much closer to the reference solution.

Table 2. Errors $E_{RMS}$ relative to the 512 × 576 subgrid solution, computed over 54 hours with 20-min sampling intervals.

| Grid size (radial × tangential) | | | | | | |
|---|---|---|---|---|---|---|
| Configuration A | | (32 × 36) | (64 × 72) | (128 × 144) | (256 × 288) | (512 × 576) |
| Station 1 | Conventional | 0.0047 | 0.0036 | 0.0014 | 0.0008 | 0.0002 |
| | Subgrid | 0.0097 | 0.0006 | 0.0012 | 0.0002 | – |
| Station 2 | Conventional | 0.6728 | 0.7150 | 0.1466 | 0.0269 | 0.0005 |
| | Subgrid | 0.0805 | 0.0282 | 0.0292 | 0.0068 | – |
| Configuration B | | | | | | |
| Station 1 | Conventional | 0.0047 | 0.0016 | – | – | – |
| | Conventional+BC | 0.0010 | 0.0017 | – | – | – |
| | Subgrid | 0.0097 | 0.0006 | – | – | – |
| Station 2 | Conventional | 0.6280 | 0.2554 | – | – | – |
| | Conventional+BC | 0.2978 | 0.1454 | – | – | – |
| | Subgrid | 0.0503 | 0.0169 | – | – | – |

## 3.2. Flooding in North Carolina due to Hurricane Florence

The North Carolina (NC) coast is characterized by an extensive barrier-island system, large sounds and estuaries, and multiple inlets, channels, and rivers that can convey water to low-lying inland locations. More than 1.2 million people live in the NC coastal region, and more than $30 billion in weather-related disasters affected the region between 2010 and 2018 (Smith 2020). Most of those disasters were related to storms, with several major hurricanes affecting the region since 2010: Irene in 2011, Arthur in 2014, Matthew in 2016, Florence in 2018, Dorian in 2019, and Isaias in 2020, each of which caused storm surge, flooding, landscape change, and damage to the built environment. Predictions of storm surge during these events should benefit from the use of subgrid corrections to represent connectivity in coastal NC. Here, we focus on Florence in 2018, which was a slow-moving storm that pushed storm surge and flooding along the open coast and far into inland regions.

### 3.2.1. Winds and water levels during Florence in 2018

Florence formed on August 31 2018 and dissipated on September 18 2018 (Stewart and Berg 2019). At its peak, Florence reached category-4 strength on the Saffir-Simpson scale with 1-minute sustained winds of 67 m/s on September 4–5. The storm's peak winds dropped below major hurricane status by 1200 UTC September 13 when the cyclone was located approximately 280 km east-southeast of Wilmington, NC. Florence made landfall near Wrightsville Beach, NC (Figure 11), at 1115 UTC September 14 as a category-1 hurricane with peak wind speed of 41 m/s (Stewart and Berg 2019). It moved slowly at and after its landfall, dumping nearly 1 m of rain in regions near Wilmington and southeast NC (Stewart and Berg 2019). Although this rainfall contributed to flooding in the week afterward, Florence's strong winds at landfall also created a significant storm surge along the open coast and within the Pamlico Sound and neighboring estuaries.

Florence's effects on coastal water levels were observed by the U.S. Geological Survey (USGS) (U.S 2021) at 34 temporary sensors and 36 high-water marks (Figure 11 and Tables 3 andB1). At each temporary sensor, time series of the water surface elevation were observed, although it should be noted that many of the temporary gauges had minimum measurable elevations, and thus water levels below these elevations could not be observed. The observed water levels had maxima of about 2.25 m along the coast between Wrightsville Beach, and about 3 m in the Neuse River estuary. These high water levels caused overtopping of barrier islands at the open coast, and they pushed up the estuaries and caused flooding of inland communities.

Table 3. Locations and identifiers for selected USGS water-level sensors during Florence. Locations are also shown in Figure 11. Model results will be explored via hydrographs (Figure 13) at these stations.

| Identifier | Station | Longitude | Latitute | Description |
|---|---|---|---|---|
| 1 | NCONS00001 | −77.1169 | 34.6875 | NC Highway 12 at Swansboro, on the White Oak River, width of about 700 m, about 5 km from Bogue Inlet and ocean |
| 2 | NCBEA11728 | −76.7482 | 35.3771 | Aurora Ferry Terminal on the Pamlico River, estuary width of about 5 km, about 25 km from Pamlico Sound |
| 3 | NCCAR12128 | −76.4561 | 34.7969 | Ferry terminal at Davis on Core Sound, width about 4 km |
| 4 | NCPAM13231 | −76.6989 | 35.0247 | NC Highway 55 at Oriental on Greens Creek, width about 400 m, on Neuse River estuary with width of about 6 km, about 20 km from Pamlico Sound |
| 5 | NCNEW12948 | −77.9258 | 34.1135 | River Road Park on the Cape Fear River, width of about 1.8 km, about 30 km from ocean |
| 6 | NCCRA12508 | −77.0189 | 35.1152 | Bridgeton across from New Bern on the Neuse River, width of about 1.5 km, about 60 km from Pamlico Sound |
| 7 | NCBEA11808 | −77.0105 | 35.5146 | Roanoke Christian Camp near Washington on the Pamlico River, width of about 1.5 km, about 55 km from Pamlico Sound |

### 3.2.2. Model setup

A digital elevation map (DEM) was developed to represent the ground surface in NC coastal regions and offshore. Topographic and bathymetric data for the NC and South Carolina coastal regions were obtained at 3-m horizontal resolution from the NOAA Digital Coast (CIRES (Cooperative Institute for Research in Environmental Sciences) 2014). Offshore bathymetric data were acquired from the NOAA bathymetric data viewer and global bathymetry and topography at 15 arc sec (SRTM15+) (National Geophysical Data Center 1998; Tozer et al. 2019). All topographic and bathymetric elevations, and all water-level data herein, are relative to the North American Vertical Datum of 1988 (NAVD88) (Zilkoski 1992). These data were blended into a DEM in a polar grid (Figure 12, top), with a shape adapted from SLOSH grids for the region (Conver et al. 2008; Glahn et al. 2009). This high-resolution polar DEM has 2368 × 3168 pixels in the radial and tangential directions, respectively.

In numerical simulations, we consider two coarse grids (Figure 12, bottom) with 148 × 198 and 296 × 396 radial and tangential cells, respectively. These grids are a result of successively de-refining the DEM grid. Table 4 gives minimum, maximum, and average distances between cell corners in the tangential $\Delta\theta$ and radial $\Delta r$ directions for the two coarse grids and the high-resolution DEM. The minimum, maximum, and average $\Delta\theta$ and $\Delta r$ for the coarser grid are 2 times larger than for the finer grid, and nearly 16 times larger than for the high-resolution DEM.

SLOSH requires atmospheric inputs to develop the surface stresses in its momentum Equations (6) and (7). Atmospheric conditions are represented within SLOSH via a parametric model (Forbes et al. 2014) with inputs of time series of storm track, radius to maximum winds, and storm pressure deficit (Jelesnianski 1992). Note that the objective of this study is to assess the performance of the subgrid model in comparison to the conventional scheme; we do not focus on obtaining the most accurate results relative to the observation, and thus we use default parameters recommended in Forbes et al. (2014). The best-track information from the National Hurricane Center (Stewart and Berg 2019) was provided as an input for the parametric model in SLOSH. Additionally, all numerical simulations used the mean high water level of Wrightsville Beach, 0.4237 m relative to NAVD88, as an initial water level, and no additional tidal forcing was included. The simulations started at 0000 UTC September 12 2018 and ran for 96 hours through landfall of the storm.

Three types of simulations were performed for each grid. The first simulation uses the conventional method, in which the SLOSH solver is run with the cell-averaged bathymetric elevation without the use of predetermined C-grid cells and with the no-slip boundary condition on wet/dry boundaries. The second simulation uses the conventional method, but with the slip boundary condition on the wet/dry boundaries (referred as the conventional + BC method). The third simulation uses the subgrid model with slip boundary, as presented in section 2.2.

### 3.2.3. Model performance at selected USGS water-level sensors

The model predictions varied significantly at the USGS water-level sensors, depending on whether the model could convey flow to locations along the coast and inland. At stations near large water bodies (either the open ocean or Pamlico Sound), the small-scale connectivity was less important, and models with the same resolution performed similarly. Station 1 (NCONS00001) was located on the White Oak River, to the northwest of Emerald Isle and about 5 km from the open ocean. At this location in the grids, the cell sizes were about 1.90 km (148 × 198) and 0.95 km (296 × 396), which was sufficient to represent the connectivity through Bogue Inlet and the sensor location at Swansboro. Similarly, Station 2 (NCBEA11728) was located on the Pamlico River estuary, about 25 km from the sound. Although this sensor was far inland, at this location in the grids, the cell sizes were about 2.06 km (148 × 198) and 1.03 km (296 × 396), which was sufficient to represent the connectivity through an estuary with a width of about 5 km. Due to this sufficient resolution, there were only minimal differences between the three model simulations on each grid at these two locations (Figure 13). At the White Oak River, the sensor observed a peak water level of about 1.9 m NAVD88, the simulations on the lower-resolution grid (148 × 198) showed a peak of about 2.4 m, and the simulations on the higher-resolution grid (296 × 396) gave a peak elevation of about 1.7 m. At the Pamlico River estuary, the sensor observed a peak water level of about 2 m, whereas the simulations showed peaks between 1.4 m and 1.6 m. Although these peaks are not a perfect

Table 4. Cell size statistics for the SLOSH grids and DEM to describe coastal NC.

| Grid size (radial × tangential) | | (148 × 198) | (296 × 396) | (2368 × 3168) |
|---|---|---|---|---|
| Tangential $\Delta\theta$ (km) | Minimum | 0.52 | 0.26 | 0.028 |
| | Maximum | 10.40 | 5.30 | 0.68 |
| | Average | 3.67 | 1.84 | 0.23 |
| Radial $\Delta r$ (km) | Minimum | 0.55 | 0.27 | 0.03 |
| | Maximum | 10.90 | 5.49 | 0.70 |
| | Average | 3.22 | 1.61 | 0.20 |

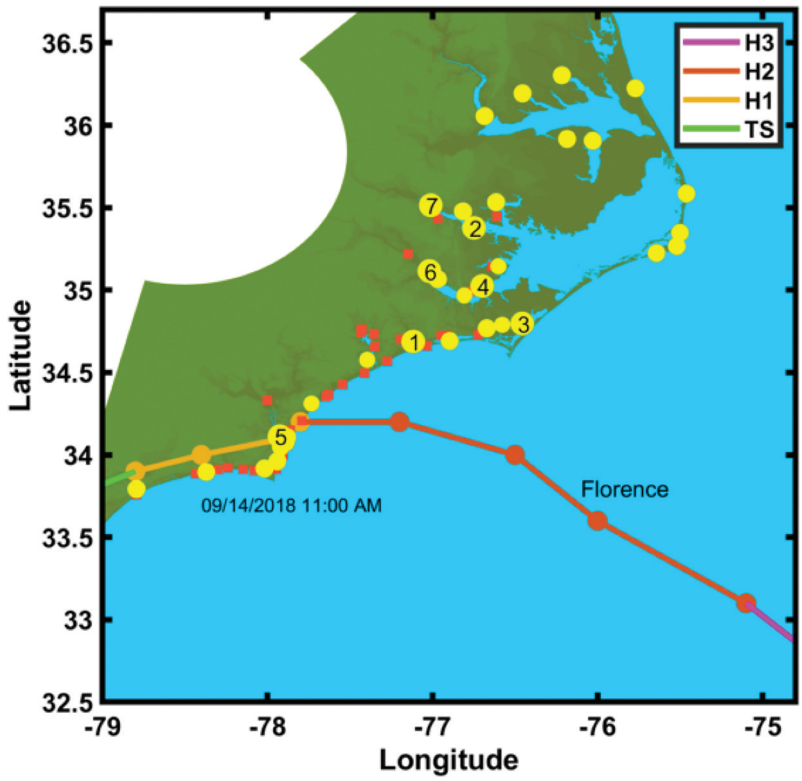


Figure 11. Track for Florence near the NC coast, with intensities on the Saffir-Simpson scale for hurricane (*H*3, *H*2, *H*1) and tropical storm (*TS*), and with circles at 6-hr intervals. Locations of USGS observations: (yellow circles) 34 temporary water level sensors; and (red squares) 36 high water marks. Selected stations described in Table 3; all stations described in Table B1.

match with observations, they show the similarity of the models at locations with sufficient resolution, and they could be improved with higher grid resolution, better atmospheric forcing, inclusion of tides and wind waves, etc.

However, at locations farther inland, the grid resolution becomes too coarse to represent flows through sounds and channels, even when they are relatively large in real terms. Station 3 (NCCAR12128) was located to the north of Cape Lookout, on the mainland side of Core Sound, where the cell sizes were about 2.38 km (148 $\times$ 198) and 1.19 km (296 $\times$ 396), which was insufficient to represent flows across Core Sound. Similarly, Station 4 (NCPAM13231) was located on the Neuse River near the opening of Green's Creek, where the cell sizes were about 2.10 km (148 $\times$ 198) and 1.05 km (296 $\times$ 396), which was insufficient to represent flows from Pamlico Sound into the estuary. Because of this, the conventional model needed the slip boundary condition to predict storm surge at these locations (Figure 13). At Core Sound, the sensor observed a peak water level of about 1.6 m, whereas the conventional model with the slip boundary condition predicted a peak of about 1.3 m on the higher-resolution grid, and the subgrid model predicted peaks of 1.4 m and 1.2 m on the lower- and higher-resolution grids, respectively. At the Neuse River, the sensor observed a peak level of about 2.4 m due to waters being pushed across the sound and into the estuary, whereas the conventional model with the slip boundary condition predicted a peak of about 2.1 m on the higher-resolution grid, and the subgrid model predicted 1.7 m and 1.9 m peaks on the lower- and higher-resolution grids, respectively. At these and similar locations, although the grid resolution is too coarse to represent the flow pathways, the slip boundary condition can allow the models to predict storm surge peaks close to the observed values.

At locations farther inland, storm surge could only be predicted with the subgrid model, due to its ability to represent flow pathways below the model scale. Station 5 (NCNEW12948, −77.9258, 34.1135) was located along the Cape Fear River, a little more than halfway between the open coast and Wilmington. This water-level sensor was elevated and could not observe the tide troughs, but it did observe a peak elevation of about 1.7 m. At this location in the grids, the cell sizes were about 2.52 km (148 $\times$ 198) and 1.26 km (296 $\times$ 396): too coarse to represent the Cape Fear River estuary, which has a width of about 2 km near this sensor. Because of this, the simulations with the conventional method do not wet at this location, and even when the slip boundary condition is added to the convention method, the peak water level of 0.6 m was too low (Figure 13). The subgrid model was able to represent the storm surge at the location, with peaks of about 1.5 m that coincide with the timing of the observed peak. The subgrid model predicts a pre-storm drawdown (of −0.5 m on the higher-resolution grid), which was not able to be observed by the sensor.

Table 5. Error statistics for predictions of peak water levels in the Florence simulations. Out of 70 combined USGS water-level sensors and high-water marks, the number of "Dry" stations is presented for each simulation. Root-mean square errors $E_{RMS}$ (Equation 31) have units of meters. Coefficients of determination $R^2$ (Equation 32) and best-fit slope $a$ indicate the quality of match between observed and predicted peak water levels. Relative times $T_{Rel}$ (Equation 33) show additional costs compared to the Conventional model.

| Grid | Simulation | Dry | $E_{RMS}(m)$ | $R^2_{all}$ | $R^2_{wet}$ | $a_{all}$ | $a_{wet}$ | $T_{Rel}$ |
|---|---|---|---|---|---|---|---|---|
| (148 × 196) | Conventional | 32 | 1.268 | −1.646 | −0.171 | 0.479 | 0.708 | 1.00 |
| | Conventional+BC | 30 | 1.267 | −1.177 | 0.213 | 0.555 | 0.838 | 1.15 |
| | Subgrid | 0 | 0.575 | 0.325 | 0.325 | 0.951 | 0.951 | 1.31 |
| (296 × 396) | Conventional | 19 | 1.063 | −0.664 | 0.238 | 0.648 | 0.859 | 1.00 |
| | Conventional+BC | 18 | 1.034 | −0.742 | 0.319 | 0.667 | 0.897 | 1.17 |
| | Subgrid | 0 | 0.545 | 0.338 | 0.338 | 0.952 | 0.952 | 1.30 |

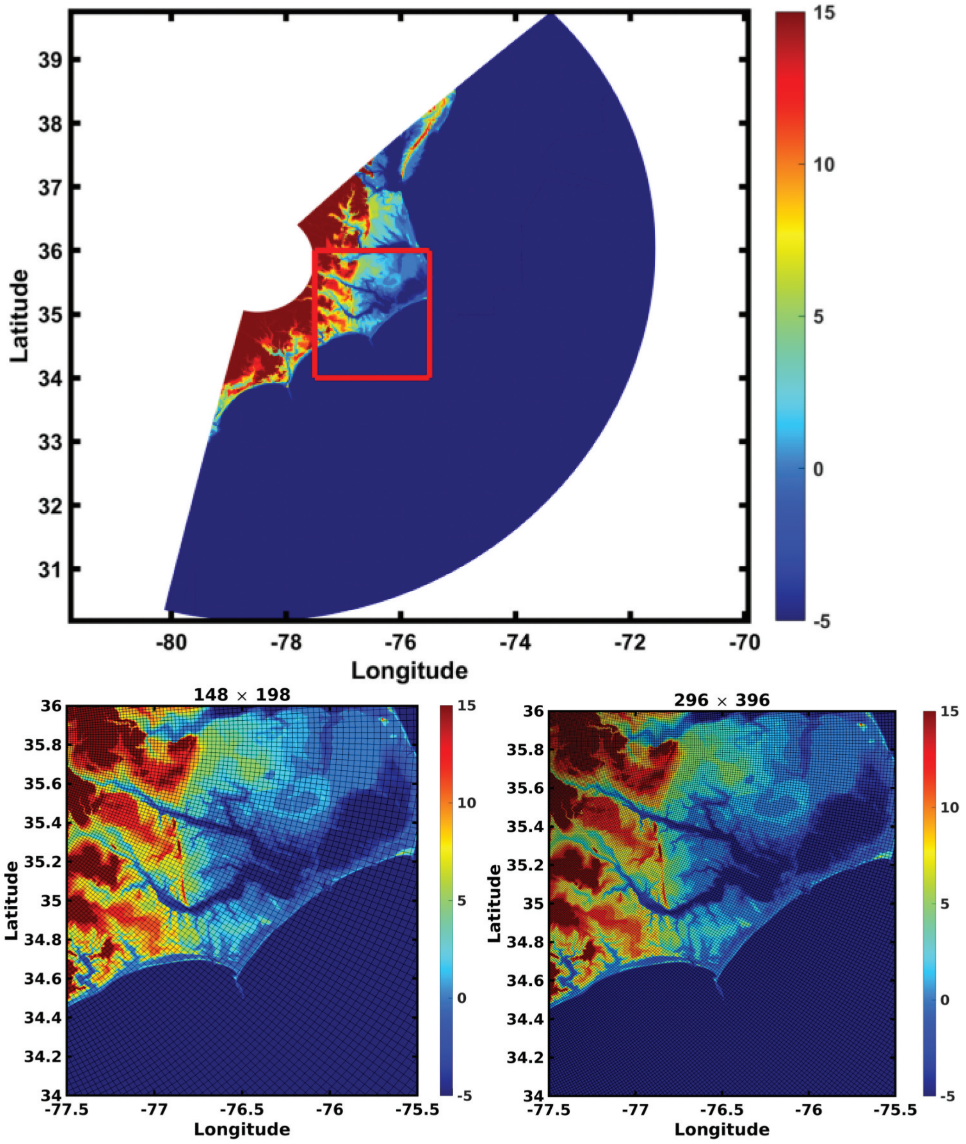


Figure 12. Ground surface elevations (m relative to NAVD88) for coastal NC, as represented by (top) high-resolution ground-surface data, and (bottom) zoom of computational grids with (left) 148 × 198 cells and (right) 296 × 396 cells.

Similarly, at the top of the estuaries, Station 6 (NCCRA12508) was located up the Neuse River estuary at New Bern, about 60 km from the Pamlico Sound, and Station 7 (NCBEA11808) was located up the Pamlico River estuary near Washington, about 55 km from the Pamlico Sound. The sensors observed peak water levels of 3.1 m and 2.2 m at New Bern and Washington, respectively, due to waters being "funneled" up the estuaries from the sound. Although these estuaries are large in real terms, with widths of 1.5 to 2 km at the sensor locations, they are small relative to the grid resolution. At the Neuse River at New Bern, the cell sizes were about 1.60 km (148 × 198) and 0.80 km (296 × 396), and at the Pamlico River at Washington, the cell sizes were about 1.68 km

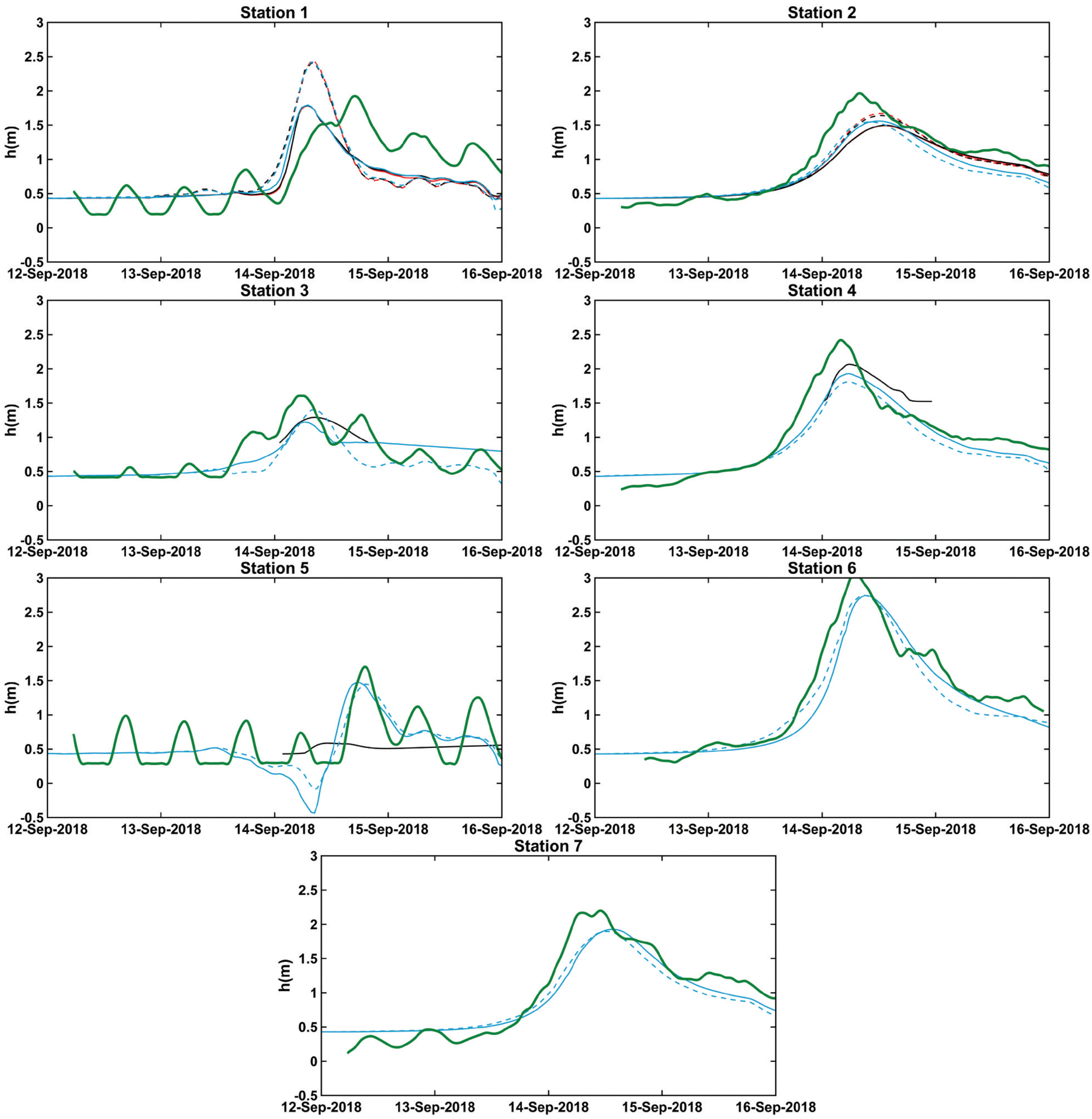


**Figure 13.** Time series of water surface elevation (m relative to NAVD88) at selected USGS water-level sensors during Florence in 2018. Observation Subgrid model (296 × 396) —; Subgrid model (148 × 198)- - - ; Conventional model (296 × 396)— ; Conventional model (148 × 198)- - - ; Conventional model with slip boundary condition (148 × 198)— ; Conventional model with slip boundary condition (148 × 198) - - -.

(148 × 198) and 0.84 km (296 × 396). Because of this, the conventional model did not predict storm surge at these locations for either grid or either boundary condition (Figure 13). However, the subgrid model did predict storm surges with peak water levels of about 2.7 m and 1.9 m, respectively. The predictions at these far-inland locations show the ability of the subgrid model to represent flow pathways below the model grid.

### *3.2.4. Model performance for peak water levels*

Florence's effects on water levels in coastal NC are described at the selected stations in the previous section, but also more comprehensively at the 70 USGS stations (34 water-level sensors and 36 high-water marks). Observed peak water levels from the sensors can be combined with the high-water marks to provide a larger inundation dataset: by comparing peak-to-peak between observations and predictions (Table 5), we can quantify the models' performance.

This comparison is challenging because the simulations with the conventional method did not predict flows at all stations, as shown anecdotally in Figure 13. Of the 70 stations, the conventional method left dry 32 stations on the lower-resolution grid (148 × 196) and 19 stations on the higher-resolution grid (296 × 396) (Table 5, third column). The slip boundary condition

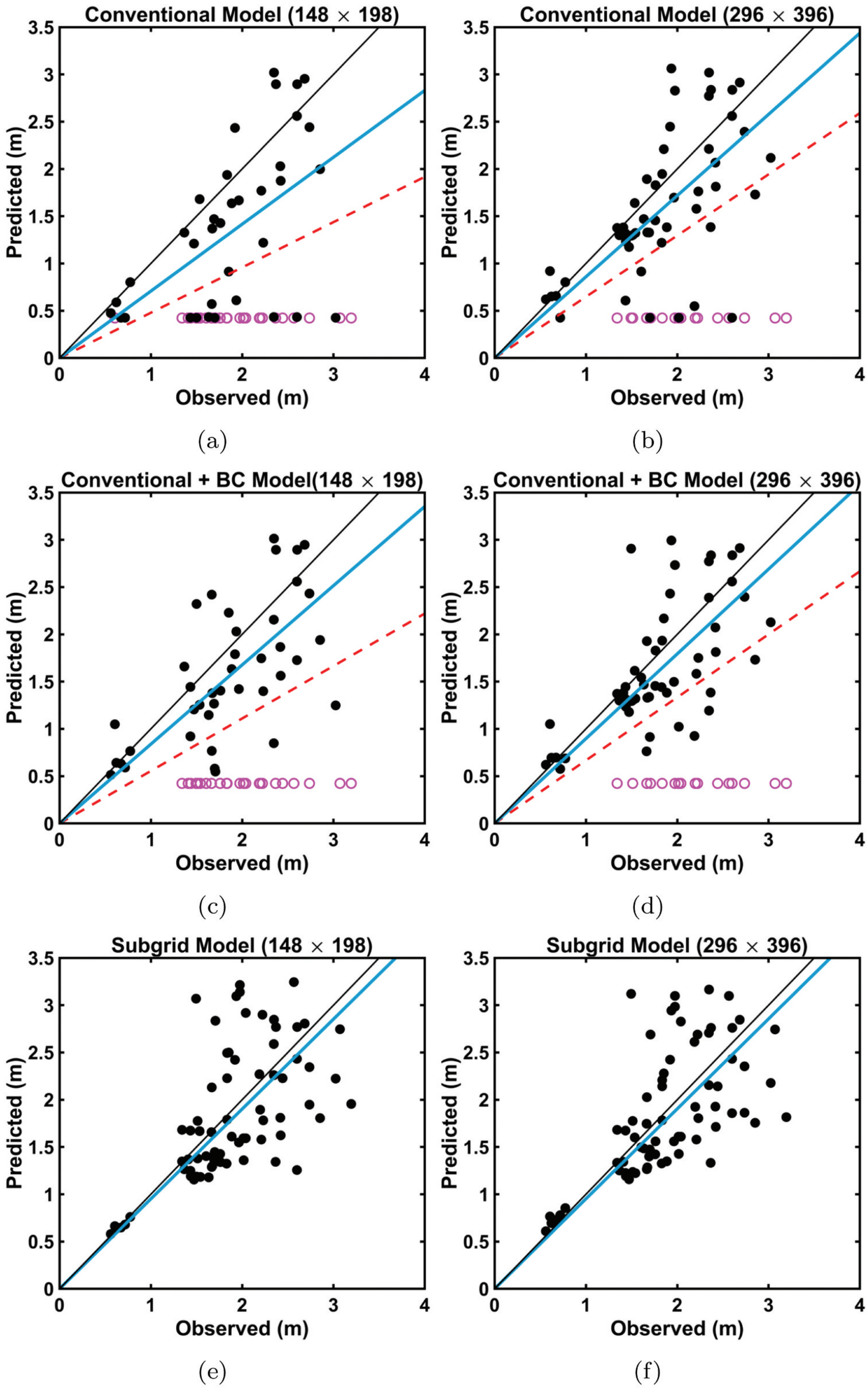


Figure 14. Comparison of observed and predicted peak water levels for Florence. The solid black circles ● are the wet stations predicted by each model. The magenta circles ○ show the dry stations predicted by each model. The black solid line (——) is 1:1 line. The blue solid line (——) is the best fit ($y = a_{\text{wet}}x$) for only the wet stations. The red dashed line (- - -) denotes the best fit ($y = a_{\text{all}}x$) for all stations.

helps incrementally, by wetting one or two additional stations. However, the subgrid model offers a significant improvement, as it predicts flows at all stations. This behavior is expected, because the subgrid corrections permit flow through features smaller than the grid scale, allowing floodwaters to reach stations that otherwise would have been predicted as dry.

For the following peak-to-peak analyses, we consider comparisons both at all stations ("all") and at stations predicted as wet in every simulation ("wet")

(Table 6, last four columns). For each simulation, three quantities are used to measure the model performance: (i) root-mean-square error ($E_{RMS}$, Equation 31), which is a measure of the magnitude of error; (ii) coefficient of determination ($R^2$), which describes how well a regression line fits a dataset:

$$R^2 = 1 - \frac{\sum (y_i - f_i)^2}{\sum (y_i - \bar{y})^2}, \tag{32}$$

where $y_i$ is the observation data for each station and $f_i$ denotes the model prediction for each station, and which is calculated relative to the 1 : 1 line; and (iii) best-fit slope ($a$ from $y = ax$ line), which indicates the overall performance of the model to predict the magnitude of the peak surge. Note that the ideal agreement based on each of these metrics correspond to $E_{RMS} = 0$, $R^2 = 1$, and $a = 1$. Two coefficients of determinations were calculated: $R^2_{all}$ for all stations, and $R^2_{wet}$ for the stations that were wetted in all simulations. In addition, two $y = ax$ lines were fitted to the data: indicator $a_{all}$ denotes the best fitted line when all stations are considered, while $a_{wet}$ shows the fitted line with dry stations excluded.

The best-fit slopes are improved with the higher-resolution grid, slip boundary condition, and subgrid model (Table 6 and Figure 14). For the conventional model and the lower-resolution grid (148 × 196), the overall best-fit slope $a_{all} = 0.479$, which includes the "dry" elevation values (at the initial MHW condition) at 32 stations. When only the wet stations are considered, its best-fit slope improves to $a_{wet} = 0.708$. This trend is repeated for the higher-resolution grid (296 × 396) and/or the slip boundary condition; for each simulation, the best-fit slope improves significantly when only the wet stations are considered. For the conventional model with the slip boundary condition on the higher-resolution grid, the best-fit slope for the wet stations is $a_{wet} = 0.897$, indicating a good match between observed and predicted peak water levels. The subgrid model offers another improvement, with best-fit slopes of 0.95 on both grids, and with water at all stations.

These trends are also repeated for the root-mean-square errors and coefficients of determination. For the conventional model on either grid, the $R^2_{all}$ values are negative, indicating a poor match between observed and predicted peak water levels. (Negative $R^2$ values are possible because it is calculated relative to the 1 : 1 line.) For the subgrid model on either grid, the $R^2$ values increase to about 0.33, indicating a better match but with significant scatter (Figure 14). For both grids, the $E_{RMS}$ values decrease with the no-slip boundary condition and the subgrid corrections, to where the subgrid model has $E_{RMS} \approx 0.55$m. These error statistics could be improved further with higher-resolution grids, fully dynamic atmospheric forcing, tides and wind waves, etc.

### 3.2.5. Computational cost

The numerical extensions introduced here do have a computational cost (Table 6), which we consider as a ratio $T_{Rel}$:

$$T_{Rel} = \frac{T_{wall-clock}}{T_{wall-clock,Conventional}}, \tag{33}$$

where $T_{wall-clock}$ is a wall-clock time for a simulation. For the higher-resolution grid, the wall-clock times are increased by a factor of about 4, as expected, because the DOFs increase by four times in the finer grid. The slip boundary condition increases the computational cost by about 16% ($T_{Rel} \approx 1.15$) relative to the conventional model. And in its current implementation, the subgrid model increases the computational cost by about 31% ($T_{Rel} \approx 1.31$) relative to the conventional model on the same grid resolutions. It is noted that the SLOSH model has been optimized for decades to provide fast forecasts during storms, whereas our numerical extensions have not been optimized.

Although the subgrid corrections introduced an additional computational cost to the model, subgrid results on coarser grids showed similar or greater accuracy than conventional methods on finer grids with and without the slip boundary condition. Thus, for a desired level of accuracy (e.g. an acceptable $E_{RMS}$ value), the subgrid model may be applied on a coarser grid, which would allow for faster computations. Therefore, considering both accuracy and computational cost, the subgrid model has an overall gain in computational efficiency.

## 4. Discussion and conclusions

In this study, subgrid corrections were implemented into the widely used SLOSH model to improve surge propagation into small channels, and other inland regions, and so to increase its range of applicability. Although improvements to friction, addition of convective accelerations, and removal of the maximum depth limitation would also be valuable additions, they are beyond the scope and resources of this work; indeed, such a level of change would create a substantially new model. Thus, we confine ourselves to two changes: (1) Incorporating subgrid corrections; and (2) Removing the no-slip wall boundary condition. These corrections were tested on various domains and showed improved accuracy both for idealized and realistic storm surge scenarios. The subgrid model can represent hydraulic connectivity and water-level calculations on coarse grids in which small hydraulic features are not resolved at the grid scale. The improvement of the results shows the ability of the subgrid model to represent small hydraulic features within partially wet cells without the use of small grid sizes as would be required in a conventional model.

Major findings are:

(1) *A slip boundary condition allows flow through small channels on a B-grid*. It can improve the results of low-resolution models in which narrow channels are not resolved at the grid level without using a staggered C-grid and predetermining the flow paths. In Configuration B of the idealized channel and bay system test case, using the slip boundary condition in the conventional approach alone reduces its $E_{RMS}$ values in the water surface elevation approximately by a factor of two at the location in the back bay where the flows can only be reached through the channel.

(2) *Subgrid corrections improve the accuracy of the model where features smaller than the grid scale are important*. We showed that a combination of the slip boundary condition on wet/dry edges with the subgrid model (FV/FV formula on the staggered B-grid with the free-slip boundary condition on the interface of wet/dry cells) represents the effects of narrow channels and small features alongside the coastlines. This advantage of the subgrid model can be seen in the real scenario of inundation induced by Hurricane Florence. The subgrid model shows improvements in all statistical quantities, which include the $E_{RMS}$ error, the $R^2$ value, and the slope of the linear best fit, used to evaluate the model's ability to predict the maximum water height at different locations. As a recap, for example, for the coarse grid with the grid sizes ranging from 0.5 to 10 km, the subgrid model improves the $R^2$ value from a negative value seen in the conventional approach to roughly 0.33.

(3) *For a given grid, introducing subgrid corrections increases the computational cost moderately; however, the subgrid corrections increase accuracy on coarser grids, leading to an overall gain in computational efficiency*. With our current implementation, the subgrid model increases the computational cost by 5 to 35% on the same grid. However, the subgrid model's predictions on coarser grids had a comparable accuracy to predictions from the conventional model on finer grids. Thus, the additional computational costs are small when compared to the accuracy offered by using coarser grids with the subgrid corrections.

These findings have implications for real-time forecast for storm surge, which can be improved with subgrid models that offer higher accuracy (via better representation of small-scale flow pathways and barriers) and/or higher efficiency (via faster run-times by using coarsened grids). These improvements allow users to automatically build an appropriate SLOSH grid based on their required applications without dependency on the existing SLOSH grids.

## Acknowledgement

The authors thank Arthur Taylor for sharing the SLOSH source code.

## Disclosure statement

No potential conflict of interest was reported by the author (s).

## Funding

This work was supported by the National Science Foundation, USA, via grants ICER 1664037 and 1664040, and through a grant from the Joint Airborne Lidar Bathymetry Technical Center of Expertise (JALBTCX), USA. Their support is gratefully acknowledged.

## References

Arakawa, Akio, and Vivian R. Lamb. 1977. "Computational Design of the Basic Dynamical Processes of the UCLA General Circulation Model." *General Circulation Models of the Atmosphere* 17 (Supplement C): 173–265.

Bates, Paul D. 2000. "Development and Testing of a Subgrid-scale Model for Moving-boundary Hydrodynamic Problems in Shallow Water." *Hydrological processes* 14 (11-12): 2073–2088. doi:10.1002/1099-1085(20000815/30)14:11/12<2073:AID-HYP55>3.0.CO;2-X.

Begmohammadi, Amirhosein, Damrongsak Wirasaet, Zachariah Silver, Diogo Bolster, Andrew B. Kennedy, and J. C. Dietrich. 2021. "Subgrid Surface Connectivity for Storm Surge Modeling." *Advances in Water Resources* 153: 103939. doi:10.1016/j.advwatres.2021.103939.

Canestrelli, Alberto, and Eleuterio F. Toro. 2012. "Restoration of the Contact Surface in FORCE-Type Centred Schemes II: Non-Conservative One-And Two-Layer Two-Dimensional Shallow Water Equations." *Advances in Water Resources* 47: 76–87. doi:10.1016/j.advwatres.2012.03.018.

Casulli, Vincenzo. 2009. "A High-resolution Wetting and Drying Algorithm for Free-surface Hydrodynamics." *International Journal for Numerical Methods in Fluids* 60 (4): 391–408. doi:10.1002/fld.1896.

Casulli, Vincenzo. 2019. "Computational Grid, Subgrid, and Pixels." *International Journal for Numerical Methods in Fluids* 90 (3): 140–155. doi:10.1002/fld.4715.

Casulli, Vincenzo, and Guus S. Stelling. 2011. "Semi-implicit Subgrid Modelling of Three-dimensional Free-surface Flows." *International Journal for Numerical Methods in Fluids* 67 (4): 441–449. doi:10.1002/fld.2361.

CIRES (Cooperative Institute for Research in Environmental Sciences). 2014. *Continuously Updated Digital Elevation Model (CUDEM)—1/9 Arc-Second Resolution Bathymetric-Topographic*.

Conver, Andrea, Julie Sepanik, Bobby Louangsaysongkham, and S. Miller. 2008. "Sea, Lake, and Overland Surges from Hurricanes (SLOSH) Basin Development Handbook V2. 0." *Silver Springs, MD: NOAA/NWS/Meteorological Development Laboratory Springs, MD: NOAA/NWS/Meteorological Development Laboratory*.

2020 Storm Surge Report, Corelogic, 2020.

Defina, Andrea. 2000. "Two-Dimensional Shallow Flow Equations for Partially Dry Areas." *Water Resources Research* 36 (11): 3251–3264. doi:10.1029/2000WR900167.

Defina, A., L. D'Alpaos, and B. Matticchio. 1994. "A New Set of Equations for Very Shallow Water and Partially Dry Areas

Suitable to 2D Numerical Models." In *Modelling of Flood Propagation Over Initially Dry Areas*, 72–81. ASCE.

Dresback, Kendra M., Randall L. Kolar, and J. Casey Dietrich. 2005. "On the Form of the Momentum Equation for Shallow Water Models Based on the Generalized Wave Continuity Equation." *Advances in Water Resources* 28 (4): 345–358. doi:10.1016/j.advwatres.2004.11.011.

Forbes, Cristina, Jamie Rhome, Craig Mattocks, and Arthur Taylor. 2014. "Predicting the Storm Surge Threat of Hurricane Sandy with the National Weather Service SLOSH Model." *Journal of Marine Science and Engineering* 2 (2): 437–476. doi:10.3390/jmse2020437.

Glahn, Bob, Arthur Taylor, Nicole Kurkowski, and Wilson A. Shaffer. 2009. "The Role of the SLOSH Model in National Weather Service Storm Surge Forecasting." *National Weather Digest* 33 (1): 3–14.

Hodges, Ben R. 2015. "Representing Hydrodynamically Important Blocking Features in Coastal or Riverine Lidar Topography." *Natural Hazards and Earth System Sciences* 15 (5): 1011–1023. doi:10.5194/nhess-15-1011-2015.

Hope, Mark E., Joannes J. Westerink, Andrew B. Kennedy, P. C. Kerr, J. Casey Dietrich, C. Dawson, Christopher J. Bender, et al. 2013. "Hindcast and Validation of Hurricane Ike (2008) Waves, Forerunner, and Storm Surge." *Journal of Geophysical Research: Oceans* 1189: 2013 4424–4460. 10.1002/jgrc.20314

Jelesnianski, Chester P. 1967. "Numerical Computations of Storm Surges with Bottom Stress." *Monthly Weather Review* 95 (11): 740–756. doi:10.1175/1520-0493(1967)095<0740:NCOSSW>2.3.CO;2.

Jelesnianski, Chester P. 1992. *"SLOSH: Sea, Lake, and Overland Surges from Hurricanes"*. Vol. 48. US Department of Commerce, National Oceanic and Atmospheric Administration, National Weather Service.

Kennedy, Andrew B., Damrongsak Wirasaet, Amirhosein Begmohammadi, Thomas Sherman, Diogo Bolster, and J. C. Dietrich. 2019. "Subgrid Theory for Storm Surge Modeling." *Ocean Modelling* 144: 101491. doi:10.1016/j.ocemod.2019.101491.

King, Ian P. 2001. "Modeling of Marshes and Wetlands." *Journal of Coastal Research* 76–87.

National Geophysical Data Center. 1998: U.S. Coastal Relief Model Vol.2 - Southeast Atlantic. NOAA National Centers for Environmental Information. 10.7289/V53R0QR5. Accessed [10/2021].

Park, Gainbi. 2021. "A Comprehensive Analysis of Hurricane Damage Across the US Gulf and Atlantic Coasts Using Geospatial Big Data." *ISPRS International Journal of Geo-Information* 10 (11): 781. doi:10.3390/ijgi10110781.

Platzek, F. W., G. S. Stelling, J. A. Jankowski, R. Patzwahl, and J. D. Pietrzak. 2016. "An Efficient Semi-implicit Subgrid Method for Free-surface Flows on Hierarchical Grids." *International Journal for Numerical Methods in Fluids* 80 (12): 715–741. doi:10.1002/fld.4172.

Platzman, George W. 1963. "The Dynamical Prediction of Wind Tides on Lake Erie." In *The Dynamical Prediction of Wind Tides on Lake Erie*, 1–44. Boston, MA: American Meteorological Society.

Roig, Lisa Catherine. 1989. *A Finite Element Technique for Simulating Flows in Tidal Flats*. University of California, Davis.

Sehili, Aissa, Günther Lang, and Christoph Lippert. 2014. "High-Resolution Subgrid Models: Background, Grid Generation, and Implementation." *Ocean Dynamics* 64 (4): 519–535. doi:10.1007/s10236-014-0693-x.

Smith, Adam. 2020. "2010–2019: A Landmark Decade of US Billion-Dollar Weather and Climate Disasters." *National Oceanic and Atmospheric Administration*.

Stelling, Guus S. 2012. "Quadtree Flood Simulations with Sub-Grid Digital Elevation Models." *Proceedings of the Institution of Civil Engineers-Water Management* 165 (10): 567–580. Thomas Telford Ltd. doi:10.1680/wama.12.00018.

Stewart, Stacy R., and Robbie Berg. 2019. "Hurricane Florence." In *National Hurricane Center Tropical Cyclone Report. Miami, FL USA: National Hurricane Center.*

Tozer, Brook, David T. Sandwell, Walter HF Smith, C. Olson, J. R. Beale, and P. Wessel. 2019. "Global Bathymetry and Topography at 15 Arc Sec: SRTM15+." *Earth and Space Science* 6 (10): 1847–1864. doi:10.1029/2019EA000658.

U.S. Geological Survey, Flood Event Viewer, https://stn.wim.usgs.gov/FEV/Retrieved 12 December 2021] (2022).

Volp, N. D., B. C. Van Prooijen, and G. S. Stelling. 2013. "A Finite Volume Approach for Shallow Water Flow Accounting for High-resolution Bathymetry and Roughness Data." *Water Resources Research* 49 (7): 4126–4135. doi:10.1002/wrcr.20324.

Welander, Pierre. 1961. "Numerical Prediction of Storm Surges." In *Advances in Geophysics*. Vol. 8, 315–379. Elsevier.

Woodruff, Johnathan L., J. C., Dietrich, D., Wirasaet, A. B., Kennedy, D., Bolster, Z., Silver, S. D., Medlin, and R. L., Kolar. (2021). "Subgrid corrections in finite-element modeling of storm-driven coastal flooding." Ocean Modelling 167: 101887.

Zachry, Brian C., William J. Booth, Jamie R. Rhome, and Tarah M. Sharon. 2015. "A National View of Storm Surge Risk and Inundation." *Weather, Climate, and Society* 7 (2): 109–117. tiles2014. doi:10.1175/WCAS-D-14-00049.1.

Zhi, Li, and Ben R. Hodges. "Model Instability and Channel Connectivity for 2D Coastal Marsh Simulations." *Environmental Fluid Mechanics* 19 (5): 1309–1338. doi:10.1007/s10652-018-9623-7.

Zilkoski, David B. 1992. "Special Report Results of the General Adjustment of the North American Vertical Datum of 1988." *Surveying and Land Information Systems* 52 (3): 133–149. David B. Zilkoski, John H. Richards, and Gary M. Young.

## Appendix A. Equations of Motion for Storm Surge With Bottom Stress

Below, the derivation of bottom stress coefficients for the governing equations of the SLOSH model is briefly summarized; we refer to Jelesnianski (1967), Jelesnianski (1992) for the full detailed account of the derivation. Welander (1961) presented a specific form of momentum equations to model the storm surge. Without the advection and horizontal mixing terms, the momentum equations in the Cartesian coordinate system with hydrostatic approximation can be written in complex form as (Welander 1961):

$$\frac{\partial w}{\partial t} = q - ifw + \frac{\partial}{\partial z'}\left(v\frac{\partial w}{\partial z'}\right) = 0, \tag{A1}$$

where

$$w = u + iv, q = -g\left[\frac{\partial(h-h_0)}{\partial x} + i\frac{\partial(h-h_0)}{\partial y}\right], i^2 = -1 \tag{A2}$$

and $(x, y)$ denotes the horizontal coordinates, $z'$ is the vertical coordinate, $v$ is vertical kinematic eddy viscosity. $f$, $g$, and $h_0$ denote the Coriolis parameter, gravity and hydrostatic height due to surface pressure, respectively.

Instead of formulating the equations with transport fields as typically done by vertically depth integrating (A1) and assuming the bottom friction as a quadratic function of transports (which would result in a more traditional form of SWE), SLOSH considers an alternative system of representing the bottom stress derived by Platzman (1963). In this system, the surface boundary condition is taken to be

$$v\left(\frac{\partial w}{\partial z'}\right)\bigg|_{z'=h} = R = x_\tau + iy_\tau \tag{A3}$$

where $R$ denotes the complex form of the (quadratic) surface wind stress while the bottom condition is formulated as:

$$v\left(\frac{\partial w}{\partial z'}\right)\bigg|_{z'=-D} = sw|_{z'=-D} \tag{A4}$$

where $s$ denotes a slip coefficient. The system is obtained from applying the transformation $z = \frac{D+z'}{D+h}$ to Equation (A2) (to make the vertical coordinate dimensionless), treating the time derivative term in (A1) as an operator, and 'formally' solving the resulting second order differential equation in $z$ with the aforementioned surface and bottom stress boundary conditions. Subsequently, the resulting solution is integrated in the vertical direction with respect to $z$ from -1 to 0, yielding:

$$\eta_v[\sigma^2 + G(\sigma)]M = Q + [1 + \lambda(\sigma)]R \tag{A5}$$

where $\eta_v = v/(D+h)^2$, $\sigma^2 = \eta_v^{-1}(if + \frac{\partial}{\partial t})$, $M = \mathrm{U} + i\mathrm{V}$ is the complex transport, and

$$G(\sigma) = \frac{\sigma^2}{\left[\frac{v\sigma^2}{s(D+h)} + \sigma\coth\sigma - 1\right]}, \quad \lambda(\sigma) = \frac{1 - \frac{\sigma}{\sinh\sigma}}{\left[\frac{v\sigma^2}{s(D+h)} + \sigma\coth\sigma - 1\right]}.$$

To obtain a simpler form amenable to numerical calculations, $G$ and $\lambda$ are estimated by truncating Taylor's expansion around $\sigma_0^2 = ifb^2/v$ (Jelesnianski 1992; Platzman 1963):

$$G(\sigma) \approx G_0(\sigma_0) + \frac{(D+h)^2}{v}G_1(\sigma_0)\frac{\partial}{\partial t};\ \lambda(\sigma) \approx \lambda_0(\sigma_0) + \frac{(D+h)^2}{v}\lambda_1(\sigma_0)\frac{\partial}{\partial t},$$

where the subscripts 0 and 1 denote the zeroth and first derivatives regarding $\sigma^2$, and the derivatives are calculated at $\sigma^2 = \sigma_0^2$. With these approximations, (A5) becomes:

$$\frac{\partial M}{\partial t} = BQ - ifAM + [C + \frac{J}{if}\frac{\partial}{\partial t}]R \tag{A6}$$

where

$$A = \frac{1 - \sigma_0^2 G_0}{1 + G_1}, B = \frac{1}{1 + G_1}, C = \frac{1 + \lambda_0}{1 + G_1}, J = \frac{\sigma_0^2\lambda_1}{1 + G_1}$$

The real and imaginary parts of (39) when the $J$ term is excluded (for more details about omitting the $J$ term, see Jelesnianski (1967)) correspond to

$$\begin{aligned}\frac{\partial \mathrm{U}}{\partial t} = &-g(D+h)(B_r\frac{\partial(h-h_0)}{\partial x} - B_i\frac{\partial(h-h_0)}{\partial y}) \\ &+ f(A_r\mathrm{V} + A_f\mathrm{U}) + C_r x_\tau - C_i y_\tau,\end{aligned} \tag{A7}$$

and

$$\begin{aligned}\frac{\partial \mathrm{V}}{\partial t} = &-g(D+h)(B_r\frac{\partial(h-h_0)}{\partial y} - B_i\frac{\partial(h-h_0)}{\partial x}) \\ &- f(A_r\mathrm{U} - A_f\mathrm{V}) + C_r y_\tau + C_i x_\tau,\end{aligned} \tag{A8}$$

## Appendix B. Measurement Locations

Table B1. Locations and identifiers for USGS observations during Florence. Locations are also shown in Figure 11. Model results were explored via hydrographs (Figure 13 at selected water-level sensors with identifiers in the first column).

| | Water-level sensors | | | High-water marks | | |
|---|---|---|---|---|---|---|
| Identifier | Station | Longitude | Latitude | Station | Longitude | Latitude |
| 2 | NCBEA11728 | −76.7482 | 35.3771 | NCBEA06921 | −76.6097 | 35.4488 |
| | NCBEA11768 | −76.8156 | 35.4772 | NCBEA11768 | −76.8147 | 35.4772 |
| 7 | NCBEA11808 | −77.0105 | 35.5146 | NCBEA26931 | −76.9721 | 35.4385 |
| | NCBEA13648 | −76.6147 | 35.5329 | NCBRU00012 | −78.4360 | 33.8867 |
| | NCBRU11851 | −78.3705 | 33.9509 | NCBRU11868 | −78.2972 | 33.9108 |
| | NCBRU12068 | −78.0179 | 33.9170 | NCBRU11888 | −78.1469 | 33.9128 |
| | NCCAR00012 | −76.6085 | 34.7892 | NCBRU11891 | −78.0821 | 33.9036 |
| 3 | NCCAR12128 | −76.4561 | 34.7969 | NCBRU11908 | −78.3738 | 33.9140 |
| | NCCAR12288 | −76.6714 | 34.7681 | NCBRU11909 | −78.2378 | 33.9217 |
| | NCCAR12409 | −76.8957 | 34.6902 | NCCAR12410 | −76.9464 | 34.7226 |
| | NCCHO12448 | −76.6840 | 36.0551 | NCCAR12412 | −77.0340 | 34.6605 |
| 6 | NCCRA12508 | −77.0189 | 35.1152 | NCCAR27260 | −76.7232 | 34.7286 |
| | NCCRA12509 | −76.9677 | 35.0659 | NCCRA27110 | −77.1486 | 35.2187 |
| | NCDAR00003 | −75.5010 | 35.3473 | NCNEW00003 | −77.9054 | 33.9979 |
| | NCDAR00008 | −75.7718 | 36.2217 | NCNEW00004 | −77.8813 | 34.0570 |
| | NCDAR12729 | −75.6432 | 35.2242 | NCNEW27302 | −78.0003 | 34.3319 |
| | NCDAR12788 | −75.4614 | 35.5851 | NCNEW27410 | −77.9197 | 33.9831 |
| | NCDAR12790 | −75.5194 | 35.2662 | NCNEW27421 | −77.9471 | 34.2140 |
| | NCNEW00002 | −77.9397 | 33.9613 | NCNEW27471 | −77.8604 | 34.1502 |
| | NCNEW12868 | −77.8792 | 34.1071 | NCNEW27844 | −77.7930 | 34.2092 |
| | NCNEW12908 | −77.9190 | 34.0507 | NCONS13048 | −77.4117 | 34.4961 |
| | NCNEW12928 | −77.8875 | 34.0779 | NCONS13108 | −77.3501 | 34.6564 |
| 5 | NCNEW12948 | −77.9258 | 34.1135 | NCONS26864 | −77.2748 | 34.5680 |
| 1 | NCONS00001 | −77.1169 | 34.6875 | NCONS27004 | −77.4349 | 34.7504 |
| | NCONS13128 | −77.3954 | 34.5762 | NCONS27007 | −77.3542 | 34.7355 |
| | NCPAM13230 | −76.8071 | 34.9675 | NCONS27014 | −77.4327 | 34.7421 |
| 4 | NCPAM13231 | −76.6989 | 35.0247 | NCONS27016 | −77.1136 | 34.7082 |
| | NCPAM13248 | −76.6008 | 35.0827 | NCONS27020 | −77.4270 | 34.7621 |
| | NCPAS13288 | −76.2164 | 36.3031 | NCONS27077 | −77.1934 | 34.7023 |
| | NCPEN00001 | −77.7330 | 34.3113 | NCPAM26921 | −76.7632 | 35.1442 |
| | NCPER00001 | −76.4544 | 36.1931 | NCPAM27039 | −76.7632 | 35.1442 |
| | NCTYR13548 | −76.1846 | 35.9878 | NCPEN00003 | −77.6282 | 34.3654 |
| | NCTYR13568 | −76.0288 | 35.9055 | NCPEN13368 | −77.5453 | 34.4248 |
| | SCHOR17780 | −78.7928 | 33.7586 | NCPEN27841 | −77.6437 | 34.3530 |
| | | | | NCONS27057 | −77.1292 | 34.6835 |
| | | | | SCHOR14333 | −78.7364 | 33.7928 |